

2007

Development of components and cells for direct conversion of energy from hydrocarbons

Prashanth Kumar Nanganuri
University of Dayton

Follow this and additional works at: https://ecommons.udayton.edu/graduate_theses

Recommended Citation

Nanganuri, Prashanth Kumar, "Development of components and cells for direct conversion of energy from hydrocarbons" (2007). *Graduate Theses and Dissertations*. 4624.
https://ecommons.udayton.edu/graduate_theses/4624

This Thesis is brought to you for free and open access by the Theses and Dissertations at eCommons. It has been accepted for inclusion in Graduate Theses and Dissertations by an authorized administrator of eCommons. For more information, please contact mschlangen1@udayton.edu, ecommons@udayton.edu.

**DEVELOPMENT OF COMPONENTS AND CELLS FOR DIRECT
CONVERSION OF ENERGY FROM HYDROCARBONS**

Thesis

Submitted to

The School of Engineering

UNIVERSITY OF DAYTON

In Partial Fulfillment of the Requirements for

The Degree

Master of Science in Mechanical Engineering

by

Prashanth Kumar Nanganuri

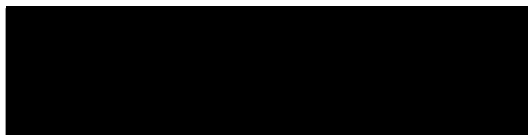
UNIVERSITY OF DAYTON

Dayton, Ohio

December, 2007

DEVELOPMENT OF COMPONENTS AND CELLS FOR DIRECT CONVERSION OF ENERGY FROM HYDROCARBONS

APPROVED BY:



Binod Kumar, Ph.D.
Advisory Committee Chairman
Group Leader, Electrochemical Power,
Metals and Ceramics Division



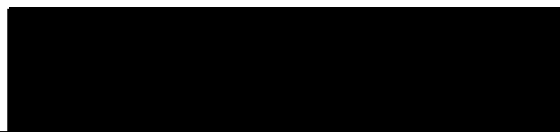
Kelly Kisson, Ph.D.
Committee Member
Professor, Mechanical and
Aerospace Engineering Department



Vinod K. Jain, Ph.D.
Committee Member
Professor, Mechanical and
Aerospace Engineering Department



Malcolm W. Daniels, Ph.D.
Associate Dean
School of Engineering



Joseph E. Saliba, Ph.D., P.E.
Dean, School of Engineering

ABSTRACT

DEVELOPMENT OF COMPONENTS AND CELLS FOR DIRECT CONVERSION OF ENERGY FROM HYDROCARBONS

Name: Nanganuri, Prashanth Kumar
University of Dayton

Advisor: Dr. Binod Kumar

In this investigation components and functional cells to be used as direct hydrocarbon solid oxide fuel cells (DHSOFC) were developed. The tape casting process was employed to make the single and bi-layers of yttria stabilized zirconia (YSZ). The bi-layers consisted of dense and porous layers of YSZ. The porous layers were made with 45 wt % of graphite pore former. A two step sintering process at 1350 °C for 2 hours and then at 1550 °C for 2 hours was employed to obtain flat layers of YSZ. The electrical properties of a porous single layer infiltrated with Cu and Cu/CeO₂ were characterized using AC impedance spectroscopy to optimize the Cu and Cu/CeO₂ to improve the performance of the cell.

After infiltrating porous side of the bi-layer YSZ with Cu/CeO₂, interlayer (YSZ+ LSM, lanthanum strontium manganate) and cathode layer (LSM) were subsequently applied on the dense side, thus making the DHSOFC. The performance of developed cells was evaluated using hydrogen as the fuel.

During the evaluation of the DHSOFC, the cells fractured because of the low mechanical strength of the cells. The mechanical strength of the cells was increased by a) adding alumina to the electrolyte and b) increasing the thickness of the electrolyte. The fuel cell made with YSZ-Al₂O₃ electrolyte and consisting of 11.85 wt% of CeO₂ and 24.16 wt% of Cu was evaluated. It exhibited peak power densities of 33 and 40 mW/cm² at 800 and 850 °C respectively. The open circuit voltage (OCV) of 0.76V and 0.83V was measured at 800 and 850 °C respectively; however, the OCV is much lower than the theoretical OCV of 1.2V of an ideal SOFC. The lower OCV is attributed to the loss resulting from the activation overpotential. In the future these DHSOFCs will be tested using the hydrocarbon fuels.

ACKNOWLEDGEMENTS

I express my gratitude to Dr. Binod Kumar, my thesis advisor, for his valuable guidance with which I could finish my research work successfully.

I am grateful to my committee members Dr. Kelly Kissock and Dr. Vinod Jain for their helpful comments. I would also like to thank Dr. Christina Chen, Dr. Joykumar Thokchom, Mr. Robert Leese and Sheila Liskany for their varied contributions and assistance. I also thank all my friends who have taken time to review this text.

TABLE OF CONTENTS

ABSTRACT	iii
ACKNOWLEDGEMENTS	V
LIST OF FIGURES	x
LIST OF TABLES	xiv
CHAPTER I	1
INTRODUCTION	1
1.1 General background.....	1
1.2 Types of fuel cells.....	2
1.3 Solid oxide fuel cell (SOFC)	2
1.4 Scope	3
CHAPTER II	5
LITERATURE REVIEW	5
2.1 Operating principle of SOFC.....	5
2.2. Triple phase boundary.....	7
2.3. SOFC thermodynamics.....	9
2.4. Operation of SOFC using hydrocarbon as fuel.....	11
2.4.1 Electrochemical oxidation of hydrocarbon fuels with Ni-based anodes.....	11

2.4.2 Electrochemical oxidation of hydrocarbon fuels with copper based anodes.....	12
2.4.3 Electrochemical oxidation of hydrocarbon fuels with Cu/CeO ₂ based anodes.....	12
2.5 Preparation of SOFC using different techniques.....	13
CHAPTER III.....	15
EXPERIMENTAL	15
3.1 Preparation of anode.....	15
3.1.1 Preparation of single layer dense YSZ tape.....	15
3.1.2 Preparation of single layer porous YSZ tape.....	16
3.1.3 Characterization of the porous YSZ layer.....	17
3.1.4 Preparation of Ni-YSZ cermet	19
a) Infiltration of Ni(NO ₃) ₂	19
i) Soaking	19
ii) Evacuation and soaking.....	19
b) Calcination... ..	21
c) Reduction	21
3.1.5 Preparation of Cu-YSZ cermet	21
a) Infiltration of Cu(NO ₃) ₂	21
b) Calcination	21
c) Reduction	22
3.1.6 Preparation of CeO ₂ -Cu-YSZ cermet.....	22
a) Infiltration of Ce(NO ₃) ₂ and Cu(NO ₃) ₂	22

b) Calcination	22
c) Reduction	22
3.2 Measurement of Electrical properties.....	23
3.2.1 Resistance	23
3.2.2 Conductivity	24
3.2.3 Transport number.....	24
3.2.4 Activation energy.....	25
3.3 Preparation of YSZ bi-layer tape.....	26
3.4 Preparation of a SOFC	27
CHAPTER IV.....	30
RESULTS AND DISCUSSION.....	30
4.1 Electrical conductivity measurement of single porous YSZ and YSZ - Ni layers.....	30
4.2 Conductivity of anodic membranes using graphite pore former.....	35
4.3 Electrical conductivity of the porous YSZ - Cu cermet.....	38
4.4 Electrical conductivity of the porous YSZ - Cu/CeO ₂ cermet.....	42
4.5 Micro-structural characterization of a YSZ - Cu/CeO ₂ Anode.....	47
4.6 Characterization and optimization of bi-layer YSZ (porous and dense).....	48

4.6.1 Optimization of sintering temperature and time.....	48
4.6.2 Optimization of graphite content in the porous layer..	54
4.6.3 Optimizing the bi-layer processing.....	56
4.7 Fabrication of direct hydrocarbon solid oxide fuel cells (DHSOFCs).....	59
4.8 Testing of direct hydrocarbon solid oxide fuel cell (DHSOFC).....	61
4.8.1 The test fixture.....	61
4.8.2 The polarization measurement of DHSOFC.....	64
CHAPTER V	68
SUMMARY AND CONCLUSIONS.....	68
REFERENCES.....	72

LIST OF FIGURES

Figure 2.1: Schematic of SOFC operating principle. (reproduced from ref 31).....	5
Figure 2.2: Schematic of Ni/YSZ anode three-phase boundary.....	8
Figure 3.1: Setup used for evacuation and soaking process	20
Figure 3.2: Nyquist plot of a typical specimen.....	24
Figure 3.3: Anode and cathode sides of the four specimens after firing at 980°C for 30 minutes.....	28
Figure 3.4: Platinum lead wire attachment to the platinized surface on electrodes before and after firing for 980°C for 30 minutes	29
Figure 3.5: SOFC cell (specimen #3) cemented onto a ceramic tube with fuel inlet and outlet tubes.....	29
Figure 4.1: Impedance spectra of porous YSZ at 600, 650, 700, 750, 800 and 850 °C.....	33
Figure 4.2: Impedance spectra of porous YSZ-Ni cermet at 607, 657, 706, 754, 803 and 851 °C.....	34
Figure 4.3: Arrhenius plots of porous YSZ and Ni-YSZ cermet specimens from 600 to 850 °C.....	35
Figure 4.4: Photographs of porous YSZ, YSZ-NiO composite, and YSZ-Ni cermet.....	36

Figure 4.5: Complex impedance plot of YSZ-Ni cermet at room temperature (25 °C).....	37
Figure 4.6: Current versus time plot of YSZ-Ni cermet at room temperature (24°C).....	37
Figure 4.7: Temperature dependence of conductivity of Cu-YSZ cermets containing 4.31, 5.89, 7.88 and 9.84 vol% of Cu after 1st time reduction.....	39
Figure 4.8: Temperature dependence of conductivity of Cu-YSZ cermets containing 15, 20, 25 and 30 vol% of Cu after 2nd reduction.....	40
Figure 4.9: Conductivity of Cu-YSZ cermets as a function of vol% of Cu at 25°C.....	41
Figure 4.10: The electronic transport number of YSZ-Cu cermet as a function of copper concentration.....	41
Figure 4.11: Arrhenius plots of YSZ – Cu/CeO ₂ anodic specimens from -35 to 25 °C.....	44
Figure 4.12: Conductivities of YSZ – Cu/CeO ₂ specimens as a function of CeO ₂ concentration at room temperature.....	45
Figure 4.13: Electronic transport number, t_e^- of YSZ – Cu/CeO ₂ specimens vs. CeO ₂ concentration.....	46
Figure 4.14: Scanning electron micrograph of a YSZ – Cu/CeO ₂ anode.....	47
Figure 4.15: SEM micrographs of the bi-layer interface at different magnifications. (a) X350, (b) X3,500 and (c) X10,000.....	49

Figure 4.16: SEM micrographs of a) the cross section showing the porous layer b) the cast surface showing open pores on the porous surface.....	50
Figure 4.17: Grain size distribution in porous and dense layers of a bi-layer specimen sintered at 1400°C/4 hours and 1500°C/1 hour.....	51
Figure 4.18: SEM micrographs of sintered bi-layer tape at higher resolution (3000 X) (a) sintered at 1400 °C for 4 hrs, (b) sintered at 1400 °C for 4 hrs and 1500 °C for 1 hr.....	51
Figure 4.19: Porosity of porous and dense layers as a function of sintering temperature.....	52
Figure 4.20: High resolution SEM micrographs of (a) dense layer and (b) porous layer. The bi-layer was sintered at 1550° for 4 hours.....	53
Figure 4.21: Porosity of the dense layer versus sintering temperature.....	54
Figure 4.22: Dried tape with 40% graphite.....	55
Figure 4.23: Porosity versus graphite content for single and bi-layers.....	56
Figure 4.24: Photographs of green bi-layer tape with 50 wt% graphite: (a) graphite side and (b) the YSZ side.....	57
Figure 4.25: Photograph of sintered disc specimen (16 mm): Row A – single layer, porous YSZ sintered at 1550°C for 4 hours; Row B – bi-layer sintered at 1550°C for 4 hours, porous layer on top; Row C - bi-layer sintered at 1350°C for 2 hours and then at 1550°C for 2 hours.	58
Figure 4.26: Photographs of anodic (after CeO ₂ and Cu infiltration) and electrolyte sides of the four specimens.....	60

Figure 4.27: Photographs of anodic (CeO_2 and Cu) and cathodic (interlayer + LSM) sides of the four specimens.....	60
Figure 4.29: Schematic design of a SOFC test fixture.....	62
Figure 4.30: Fixture components: (a) unassembled (b) assembled (c) fuel cell cemented to the fixture.....	63
Figure 4.31: I – V curve and power density curve of DHSOFC (Cu and CeO_2 anode) operated at 800°C.	66
Figure 4.32: I – V curve and power density curve of DHSOFC (Cu and CeO_2 anode) operated at 850°C.	67

LIST OF TABLES

Table 2.1: Standard cell potential, E° , for various fuels at 973 K and 1073 K...	10
Table 2.2: Overview of some common thin and thick film SOFC fabrication technique.....	14
Table 3.1: Dense YSZ tape cast formulation.....	16
Table 3.2: Porous YSZ tape cast batch formulation.....	17
Table 3.3: $\text{Ni}(\text{NO}_3)_2$ infiltration parameters.....	20
Table 4.1: Resistances of specimens at temperature ranging from 600 to 850 °C.....	32
Table 4.2: Volume percent composition of the Cu/CeO ₂ -YSZ anode specimens.....	43
Table 4.3: Atom concentration (%) at various points in the micrograph of figure 4.14.....	48
Table 4.4: Porosity and density of YSZ after sintering at 1550°C for 4 hours.....	56
Table 4.5: Geometrical Characteristics of YSZ single and bi-Layers before and after sintering.....	58
Table 4.6: Properties and constitution of direct Oxidation SOFC bi-layer specimens.....	59

CHAPTER I

INTRODUCTION

1.1 General background

A fuel cell is an electrochemical device that converts chemical energy directly into electrical energy when fuel and oxidant are supplied. Advantages of fuel cells are many. Fuel to energy conversion efficiency is very high because it directly converts chemical energy to electrical energy. Unlike turbines, these are not subjected to Carnot-cycle limitations. Moreover this efficiency is independent of size and variability of loads. Absence of moving parts makes the fuel cell operations noiseless; the only noise arises from auxiliary equipment. Fuel cells do not produce significant quantities of NO_x , and SO_x . Fuel cells are useful for applications that require both low and high power outputs.

The First demonstration of Fuel cell was made by William Grove in 1839 but fuel cells have only recently attracted much commercial interest. In the 1960s, NASA employed fuel cells to generate electric power for spacecraft. The market for fuel cells has remained confined to space programs for the last four decades because of excessive unit cost of power generation. Recent initiatives on energy uses and conservation have restored interest in fuel cells.

1.2 Types of fuel cells

Five types of fuel cells are currently being used or under development. They are the alkaline fuel cell (AFC), the proton exchange membrane fuel cell (PEMFC), the molten carbonate fuel cell (MCFC), the phosphoric acid fuel cell (PAFC), and the solid oxide fuel cell (SOFC). These fuel cells are characterized by the type of electrolyte they use and consequently the operating temperature which ranges from ambient temperature to 1000 °C.

1.3 Solid Oxide Fuel Cell (SOFC)

Among the varieties of fuel cells, solid oxide fuel cells (SOFC) are currently being developed with greater emphasis in a wide spectrum of power generation sizes. The key feature of SOFC lies in its all-ceramic components. The use of solid electrolyte in SOFC eliminates material corrosion and thereby permits unique cell design to have improved performance. However, the use of ceramic electrolyte necessitates high operating temperature (600-1000 °C) to achieve high electrical conductivity. This means that high electrochemical reaction rates at electrodes can be achieved without the use of expensive catalysts, and also high temperature operation produces high quality byproduct heat which can be used in cogeneration and bottoming cycles. Moreover, the exhaust heat can be utilized in various industrial processes. The utilization of waste heat in the bottoming cycle for electric power generation results in a very high overall fuel to energy conversion efficiency ($\approx 90\%$).

Conventional SOFC designs generally use either hydrogen or internally reformed hydrocarbons as the fuel. The reforming process is complex and for

higher hydrocarbons, such as gasoline and diesel fuels, a separate fuel-processing unit is required. Although hydrogen is often referred to as being the ideal fuel of the future SOFC, there are a number of problems relating to hydrogen generation and storage that must be overcome before it can be implemented on a wide scale. Unlike hydrocarbon fuels, hydrogen is not readily available and an entire infrastructure will need to be built in order to use it on wide scale. Significant problems associated with hydrogen storage are yet to be solved. For all of these reasons, it would be advantageous if one could operate SOFC directly on a hydrocarbon fuel without the need of the intervening reforming steps and purification of gases to obtain hydrogen. This type of fuel cell is called direct hydrocarbon solid oxide fuel cell (DHSOFC).

In conventional SOFC anodes are Ni-based cermet. Since Ni is an excellent catalyst for the formation of graphite filaments from dry hydrocarbons at elevated temperatures, the use of hydrocarbon fuels in SOFC with an anode containing Ni results in carbon deposition and rapid, irreversible cell deterioration (1-4). Therefore Ni cannot be used in the anode cermet for direct hydrocarbon solid oxide fuel cells.

1.4 Scope

The aim of the present work is to develop anode materials that are useful for the direct hydrocarbon solid oxide fuel cell. Metallic copper is known to prevent carbon filament formation at high temperatures (500 – 1000 °C). Ceria (CeO_2) is an excellent catalyst for the oxidation of hydrocarbons. Therefore, a combination of Cu and CeO_2 can be employed to replace Ni to utilize hydrocarbons directly in SOFC. For this work SOFCs were produced

using the tape casting method and this thesis presents, discusses and analyses the composition optimization of the anode cermet for DHSOFC along SOFC performance data.

CHAPTER II

LITERATURE REVIEW

2.1 Operating principle of SOFC

The operating principles of an SOFC are schematically shown in Figure 2.1. Like all fuel cells, the SOFC consists of three main components: a cathode (or air electrode), an anode (or fuel electrode), and an electrolyte. The distinguishing feature of an SOFC is that the electrolyte is an oxygen ion-conducting ceramic membrane.

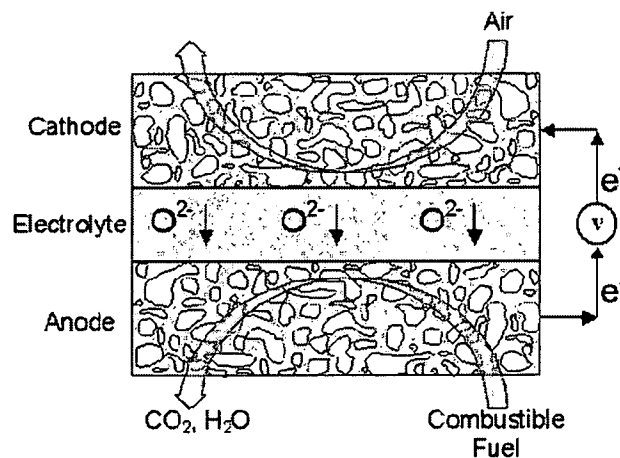


Figure 2.1: Schematic of SOFC operating principle. (reproduced from ref 32.)

The electrolyte must be dense in order to separate the fuel and air compartments of the fuel cell, and it must retain its high ion conductivity and low electronic conductivity over a very wide range of oxygen fugacities, from values close to 1 atm at cathode side to values that could be below 10^{-20} atm at the anode. The material most often used as the electrolyte is

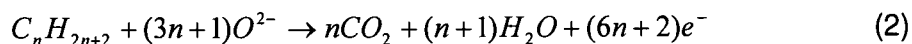
yttria-stabilized zirconia (YSZ) (5). While other materials having higher ionic conductivities at lower temperatures are being considered, most of these materials do not have high stability and low electronic conductivity at low partial pressure of oxygen ($p(\text{O}_2)$). Since decreased operating temperatures simplify the materials requirements in other parts of the SOFC, there is a trend toward using very thin electrolytes to minimize conduction path supported on one of the electrodes.

During an operation of SOFC, molecular oxygen is reduced to oxygen anions using electrons supplied from an external circuit at the cathode, according to the following reaction:



In addition to being able to catalyze the dissociation and ionization of O_2 , the material used for the cathode must be electronically conductive in the presence of air at high temperature (a property found primarily in metals and electronically conductive oxides). Significant ionic conductivity is also desirable for extending the reaction zone well into the cathode since the ions must ultimately be transferred to the electrolyte. Since precious metals are prohibitively expensive when used in quantities sufficient for providing electronic conductivity, essentially all SOFC prototypes use perovskite-based cathodes, with the most common material being a Sr-doped LaMnO_3 (LSM) (6). Finally, the cathode material must have a coefficient of thermal expansion (CTE) similar to that of electrolyte.

Driven by the difference in oxygen chemical potential between fuel and air compartments of the cell, oxygen anions migrate through the electrolyte to the anode where they are consumed by oxidation of the fuel according to eq 2.



The electrons released by this reaction flow through an external circuit to the cathode to complete the circuit. Analogous to the cathode, the anode must be catalytically active for the oxidation reaction and retain sufficient electronic and ionic conductivities. For example, with the current state-of-the-art anode materials, which are Ni-YSZ, ceramic-metal (cermet) composites, Ni provides the catalytic activity and electronic conductivity, while the YSZ component provides ionic conductivity and a thermal expansion match with the YSZ electrolyte. While metals other than Ni can be used in the anode, Ni is almost universally used because it is inexpensive, has excellent mechanical and electrical properties, and is a good steam-reforming catalyst.

2.2. Triple phase boundary

The electrochemical reactions in both the electrodes can only occur at the three-phase boundary (TPB), which is defined as the point or line at which the electrolyte, the electron-conducting metal phase, and the gas phase all come together. A schematic of the region between the electrolyte and the anode where the TPB exists is shown in Figure 2.2. If there is a breakdown in connectivity in any one of the three phases, the reaction cannot occur. If any of the three species participating in the reaction i.e. ions from or to the electrolyte, molecules from the fuel source or oxidant and electrons from the electrode are absent, the reaction will not proceed and the performance of the cell will be degraded. While the structure and composition clearly affect the size of the TPB, various theoretical and experimental methods have been used to estimate that, under normal conditions, the region in which the TPB

exists extends no more than approximately $10\text{ }\mu\text{m}$ from the electrolyte into the electrode (7-13)

The TPB concept has important implications for optimization of both anodes and cathodes. To facilitate transfer of O^{2-} to or from the electrolyte, it is necessary to have fingers of the electrolyte material extending from the electrolyte into the electrode. A detailed analysis of the role of these fingers has been carried out for cathodes (10, 14-16) and similar concepts are also applicable to the anode. It is important to note that the electrolyte material within the electrode is only effective if it is sintered and connected to the electrolyte membrane. When oxide particles are simply pressed together at low temperatures, there will be large grain-boundary resistances that will prevent the flow of oxygen ions. Removing the grain-boundary resistance between YSZ particles typically requires high sintering temperatures ($1400\text{-}1500\text{ }^{\circ}\text{C}$). The most commonly used material for the cathode is a

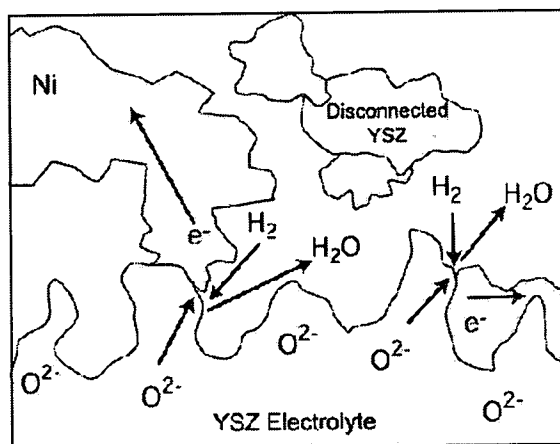


Figure 2.2: Schematic of Ni/YSZ anode three-phase boundary

composite of YSZ and lanthanum strontium manganate (LSM), $\text{La}_{1-x}\text{Sr}_x\text{MnO}_3$. The primary reason for using LSM, rather than materials such

as $\text{La}_{1-x}\text{Sr}_x\text{FeO}_3$ (LSF) or $\text{La}_{1-x}\text{Sr}_x\text{CoO}_3$ (LSC) that exhibit a better performance, is that LSM-YSZ mixtures can be heated to higher temperatures before undergoing a solid-state reaction with YSZ (17-20).

2.3. SOFC thermodynamics

The maximum electrical energy available from a fuel cell is determined by the Gibbs free energy difference, ΔG across the electrolyte membrane. For hydrogen as fuel and oxygen as reactant, forming water as reaction product (equation 3), the thermodynamic equilibrium voltage, E is expressed by equation 4 which is also known as the Nernst equation where $P(\text{H}_2)$, $P(\text{O}_2)$ and $P(\text{H}_2\text{O})$ are partial pressure of hydrogen, oxygen and water respectively.



$$E = E^\circ + (RT/2F) \ln \{ P(\text{H}_{2\text{anode}}) P(\text{O}_{2\text{cathode}})^{1/2} / P(\text{H}_2\text{O}_{\text{anode}}) \} \quad (4)$$

At the temperatures of interest for SOFC applications, the standard potentials for oxidation, E° , H_2 , CO and hydrocarbon fuels are shown in table 2.1. Since E° for H_2 is strongly temperature dependent (decreases with increasing temperature) than the E° for hydrocarbons, the thermodynamic advantage for hydrocarbon fuels is apparent at higher temperatures. With this information it can be stated that the thermodynamic efficiency of a fuel cell operating directly on hydrocarbon fuels is significantly higher.

Table 2.1: Standard cell potential, E° , for various fuels at 973 and 1073 K

fuel	E° , 973 K (V)	E° , 1073 K (V)
hydrogen	1.01	0.98
carbon monoxide	0.99	0.98
methane	1.05	1.04
<i>n</i> -butane	1.13	1.12
toluene	1.13	1.12
<i>n</i> -decane	1.14	1.13

In an ideal fuel cell, the thermodynamic efficiency is equal to $\Delta G/\Delta H$ where ΔG is Gibbs free energy and ΔH is the change in enthalpy (21). In practice, the energy losses in the fuel cell are significantly higher. To calculate the electrical energy produced/generated from a given amount of fuel using a fuel cell, one can simply take the product of the number of electrons produced times change in the potential of these electrons. Therefore, for a fixed amount of fuel, energy losses occur if either the number of electrons that are produced decreases or if the cell potential decreases. A fuel utilization of 90% is a typical goal in an SOFC, implying that 10% of the fuel is simply lost without producing electrons. In addition, the potential of a fuel cell (V), given by Eq. 5, is usually much lower than the Nernst potential

$$V = E^\circ - \eta_{\text{ohmic}} - \eta_{\text{cathode}} - \eta_{\text{anode}} \quad (5)$$

Where η_{ohmic} , η_{cathode} and η_{anode} are losses from electrolyte ($i \cdot R_{\text{electrolyte}}$), cathode and anode respectively. In an SOFC the ohmic loss, η_{ohmic} is significant and normally minimized by decreasing electrolyte thickness and thus resistance.

2.4. Operation of SOFC on hydrocarbon fuels

There are two basic strategies for directly converting hydrocarbons to electrical energy in an SOFC. The first involves using conventional, Ni-based anodes under conditions in which carbon does not form. This approach necessitates operation of the fuel cell under thermodynamically favorable parameters. The second strategy involves using alternate anode materials that do not catalyze carbon formation.

2.4.1. Electrochemical oxidation of hydrocarbon fuels with Ni-based anodes

Barnett and co-workers reported that it might be possible to utilize hydrocarbons directly in SOFC with Ni-based anodes (22-26). They reported that there is a narrow temperature window, between 550 and 650 °C, in which carbon is not as stable while using methane as the fuel. They also suggested that even when carbon does form on Ni-based anodes, it may be possible to remove this carbon as fast as it forms if the O^{2-} flux from the electrolyte is sufficient (22, 24, 25).

The results with methane shows that it may be possible to operate a fuel cell with hydrocarbon fuels using Ni-based anodes and low steam contents in a laboratory environment but the approach is not practical. To operate in a very narrow temperature window to maintain stability any temperature excursions in the stack that might occur during increased loading would be unacceptable. It is also not possible to prevent carbon formation by high O^{2-} flux through electrolyte. O^{2-} can remove carbon near the triple-phase boundary, a region that extends no more than approximately 10 μ m from the electrolyte interface. This implies that the O^{2-} flux can have little influence on

the carbon removal from the Ni cermet. Therefore, Ni cannot be used in the anode for commercially viable direct-hydrocarbon solid oxide fuel cells.

2.4.2 Electrochemical oxidation of hydrocarbon fuels with copper based anodes

To avoid the formation of carbon is to replace the Ni with a metal that is not a catalyst for carbon formation. Unfortunately, there is no metal replacement for Ni that has acceptable catalytic and electrical properties, so that it is necessary to make compromises based on the other performance requirements to select the replacement for Ni. First, the metal must be stable, both to the high operating temperatures and to the range of $p(\text{O}_2)$ that the anode is subjected to. Metals such as Mo with low melting temperatures are excluded as they would be oxidized by water in the anode compartment. Second, because the metals must be present in quantities sufficient to provide electronic conductivity, precious metals are excluded because of cost. Therefore, Cu which is known to be a poor catalyst for C-C bond formation and which is catalytically inert can replace Ni in SOFC operating on direct hydrocarbons. Because Cu is a relatively poor oxidation catalyst, another material or component must be added to the anode for hydrocarbon oxidation.

2.4.3 Electrochemical oxidation of hydrocarbon fuels with Cu/ Ceria (CeO_2) based anodes

Ceria is a good oxidation catalyst. It was shown that addition of ceria to a Cu-YSZ cermet significantly enhances the performance of the cell, especially with hydrocarbon fuels (27-29). Unlike transition metals, ceria does not promote C-C bond formation, and therefore, does not tend to catalyze formation of carbon deposits. Because of this inherent property, ceria is also

used in self-cleaning ovens. It was also shown that performance of the fuel cells with Cu-ceria-YSZ anodes was significantly better when the anodes are fabricated by first impregnating the porous YSZ matrix with ceria and then with Cu added in later steps. Cells in which the Cu was added first, or in which the Cu and ceria were added simultaneously, show significantly lower power densities (30). This implies that the ceria must be in direct contact with the electrolyte for it to be effective.

A significant research activity has taken place to identify oxides with properties similar to ceria. It was found that ceria is the best oxide and the catalytic activities decreased in the following order: Eu_2O_3 , Tb_4O_7 , Pr_6O_{11} , Sm_2O_3 , Yb_2O_3 , ZrO_2 and La_2O_3 (31).

In addition to its catalytic properties, ceria is known to be an ionic conductor, a property which is important for the SOFC anode.

2.5 Preparation of SOFC using different techniques

The general overview of thin and thick film deposition methodologies for fabricating SOFCs is presented in Table 2.2. Depending on the thickness of the electrode or electrolyte layers and economic considerations, the choice of SOFC fabrication technique can be selected.

In the present work effort, it was decided to use tape casting method for several reasons. First of all it is a widely accepted method to process ceramic fuel cell assemblies. Also, it is an easily scalable method and an in-house facility was available. It is also suitable for cathode and anode fabrication due to the fact that thin films are not necessarily required.

Table 2.2: Overview of some common thin and thick film SOFC fabrication techniques

Technique	Deposition rate or thickness	Costs	Comments
Vapor Phase			
CVD	1 - 10 $\mu\text{m/h}$	Expensive equipment	Use of organic precursor materials possible, high temperature necessary
PVD	0.25 - 2.5 $\mu\text{m/h}$	Expensive equipment	Dense and crack-free coating, low deposition temperature, but low deposition rate
Laser Ablation		Expensive equipment	Intermediate deposition temperatures, low deposition rate
Spray Pyrolysis	5 - 60 $\mu\text{m/h}$	Economical	Upscaling possible, robust
Liquid Phase			
Sol-Gel	~0.5 - 1 μm for each coating	Economical	Very thin films, crack formation, many process parameters
Solid Phase			
Tape Casting	25 - 200 μm	Economical	Upscaling possible, robust
Slip Casting	25 - 200 μm	Economical	Robust, crack formation, slow
Tape calendaring	5 - 200 μm		Upscaling possible
Screen Printing	10 - 100 μm	Economical	Upscaling possible, robust, crack formation

CHAPTER III

EXPERIMENTAL

3.1 Preparation of anode

Anode is a critical component of the solid oxide fuel cell (SOFC) and also for this investigation. It is expected to carryout direct electrochemical oxidation of hydrocarbon fuels. The technical requirements of the anode are many. The requirements include chemical stability in a side range of oxygen partial pressures at high temperatures (600-1000 °C), must be able to provide large surface area so that the oxidation can be carried out efficiently and also must be mechanically robust to withstand typical heating and cooling rates.

3.1.1 Preparation of single layer dense YSZ tape

YSZ powder (1 – 45 μm), fish oil, xylene and alcohol in proportions shown in Table 3.1 were mixed and tumbled for 24 hours in a glass jar. A binder and a mixture of plasticizers were subsequently introduced into a glass jar and the mixture was tumbled for another 24 hours. Slurry obtained after total tumbling time of 48 hours was cast onto a Mylar sheet using a firm and clean doctor blade. The height of the doctor blade can be set according to the required thickness of the tape. The cast tape was dried for 24 hours at room temperature, and it shrank nearly 50-65 %. The green tape obtained by this processing technique was flexible, easy to handle and can be cut into desired geometry. Specimens of desired geometry were then subjected to binder

burnout and sintering processes. For a typical binder burn out a slow heating rate of $0.5\text{ }^{\circ}\text{C min}^{-1}$ was practiced from 25 to $500\text{ }^{\circ}\text{C}$ to avoid warping and pin holes. The heating rate was increased to $1^{\circ}\text{C min}^{-1}$ from 500 to $1350\text{ }^{\circ}\text{C}$ and soaked at this temperature for 2 hours. It was cooled down to room temperature at the rate of $3\text{ }^{\circ}\text{C per minute}$. Thereafter, the specimen was heated at the rate of $1\text{ }^{\circ}\text{C per minute}$ to $1550\text{ }^{\circ}\text{C}$. After sintering at this temperature for 2 hours, it was cooled down to room temperature at the rate of $3\text{ }^{\circ}\text{C per minute}$.

Table 3.1: Dense YSZ tape cast formulation

Materials	Wt%	Weight (g)	Weight (ml)
Part-I Milling for 24 hours			
YSZ	61.95	40.27	20 wt%
Menhaden fish oil	1.24	0.81	
Xylene	15.31	9.95	11.38
Alcohol	15.31	9.95	12.87
Part-II Milling for another 24 hours			
Butyl benzyl phthalate (plasticizer I)	1.55	1.01	0.71
Extra plasticizer I			0.70
Poly alkylene glycol (plasticizer II)	1.55	1.01	0.71
Extra plasticizer II			0.70
Polyvinyl butyl (binder)	3.09	2.01	
Total	100	65.01	

3.1.2 Preparation of single layer porous YSZ tape

The only difference in making dense and porous layer is pore former. A pore former is required in preparing YSZ tape. To get porous YSZ tape, the procedure used to get dense YSZ tape was followed as discussed in section 3.1.1. Ingredients and their proportions are tabulated in Table 3.2. The green tape obtained by this was also flexible, easy to handle and can be cut into

desired geometry. Specimens of desired geometry were then subjected to a binder burnout and sintering processes. During the binder burnout process, pore former burns out leaving voids called pores. Heating and cooling rates for typical binder burnout was same as discussed in section 3.1.1.

Two different pore formers, rice flour and graphite, were used separately to prepare porous YSZ. The two pore formers produced specimens with different microstructures. The results will be discussed in detail in results and discussion section.

Table 3.2: Porous YSZ tape cast batch formulation

Materials	Wt%	Weight (g)	Weight (ml)
Part-I Milling for 24 hours			
YSZ	34.07	20.44	
Graphite or rice flour-300 mesh	27.88	16.73	45%
Menhaden fish oil	1.24	0.81	
Xylene	15.31	9.95	11.38
Alcohol	15.31	9.95	12.87
Part-II Milling for another 24 hours			
Butyl benzyl phthalate (plasticizer I)	1.55	1.01	0.71
Extra plasticizer I			0.70
Poly akylene glycol (plasticizer II)	1.55	1.01	0.71
Extra plasticizer II			0.70
Polyvinyl butyl (binder)	3.09	2.01	
Total	100	65.01	

3.1.3 Characterization of the porous YSZ layer

The porosity and pore structure of the porous YSZ layer is of significant importance as an anodic component, such that Ni or Cu can be deposited in these pores so that they form triple phase boundaries (TPB) for direct oxidation of fuels. In view of these requirements, the porosity has been

characterized by water saturation procedure as presented in Illustration 3.1. The porous single layer tapes are soaked in water and a determination of the volume of the soaked water allows a quantitative measurement of the volume of interconnected pores. The isolated pores remain hidden and unaccounted for. The interconnected pores will allow infiltration of the anodic solution, such as copper nitrate or nickel nitrate.

A combination of experimental data by the water saturation technique and their comparison with theoretical porosity help us determine the nature of the pores.

$$\text{Porosity} = \frac{\text{Volume of Pores}}{\text{Volume of Specimen}}$$

$$\text{Volume of pores (cc)} = W_2 - W_1$$

$$\text{Volume of the specimen} = (W_1 - W_0) \text{ or } \frac{W_1}{d}$$

where W_2 = weight of the water soaked specimen in air

W_1 = weight of specimen in air

W_0 = weight of the specimen in water

d = density of the specimen.

$$\text{Porosity (\%)} = \frac{W_2 - W_1}{W_1 - W_0} \times 100 \text{ or } \frac{(W_2 - W_1)d}{W_1} \times 100$$

Illustration 3.1: Porosity definition and method for its measurement.

3.1.4 Preparation of Ni-YSZ cermet

a) Infiltration of Ni (NO₃)₂

Nickel nitrate solution was prepared by dissolving the salt in distilled water. Later on the solution was impregnated into porous YSZ using two different techniques.

- i) Soaking
- ii) Evacuation and soaking

i) Soaking

Porous YSZ specimens were immersed in the solution for 30 minutes. Capillary force is the driving force for the solution to get into the pores of the specimens. More solution can get into specimens with higher porosity than the specimens with lower porosity. Therefore, the specimens have to be highly porous to accommodate large amount of solution. The process of infiltration and calcination were conducted several times to impregnate required amount of the Ni catalyst into the specimens.

ii) Evacuation and soaking

In this case infiltration process was carried out in a vacuum. The experimental set up for vacuum infiltration is shown in figure 3.1. The specimen was placed in vacuum chamber and subsequently vacuum was applied using mechanical pump. The anodic solution was stored in a container above the vacuum chamber. After the vacuum chamber with specimen was evacuated for 15 minutes, the anodic solution was introduced into the vacuum chamber and allowed to fall onto the specimens drop by drop. The purpose for this infiltration technique was to infiltrate more amount

of solution into the specimens so that number of infiltrations could be decreased.

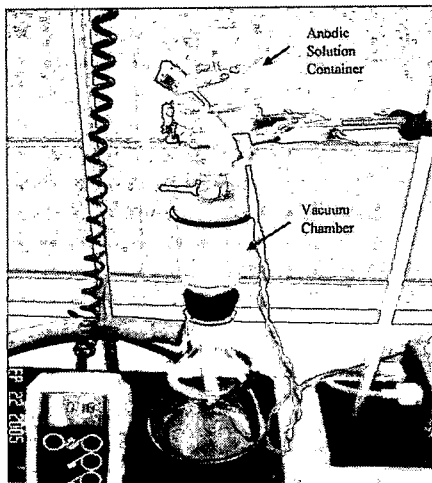


Figure 3.1: Setup used for evacuation and soaking process.

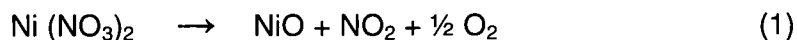
Experimental data obtained from the two experimental techniques is presented in Table 3.3. It is evident that evacuation does help the infiltration process but not to a large extent as the specimen infiltrated nine times gained about an average of 0.77%. Therefore, only the soaking infiltration technique was used from hereon for infiltrating catalyst instead of evacuation and soaking infiltration technique.

Table 3.3: $\text{Ni}(\text{NO}_3)_2$ Infiltration parameters

Specimen No.	Soaking			Evacuation and Soaking		
	Porous Specimen wt (gm)	Wt. of the Specimen after Calcination (gm)	Wt.% NiO	Porous Specimen wt (g)	Wt. of the Specimen after Calcination (gm)	Wt.% NiO
1	0.120	0.184	34.783	0.118	0.187	36.898
2	0.127	0.221	42.534	0.112	0.195	42.564
3	0.114	0.206	44.660	0.128	0.232	44.826

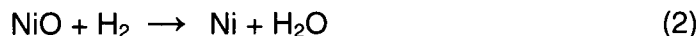
b) Calcination

After every infiltration, the specimens were calcined at 500 °C for 1 hour. During this process, nickel nitrate decomposed to nickel oxide according to the equation 1.



c) Reduction

After several times of infiltration and calcinations the specimens were left out with NiO. These specimens were reduced in hydrogen atmosphere at 860 °C for 2 hours leaving Ni in the specimens (equation 2).



3.1.5 Preparation of Cu-YSZ cermet

a) Infiltration of Cu(NO₃)₂

To infiltrate copper nitrate solution into the specimens only soaking technique was used for the reasons explained in the previous section.

b) Calcination

Every time after the infiltration with copper nitrate solution, the specimens were calcined at 350 °C for 30 minutes. During this process, copper nitrate decomposed to copper oxide according to the equation 3.



c) Reduction

After the completion of infiltration and subsequent calcination processes, the specimens were reduced in hydrogen atmosphere at 600 °C for 8 hours. During this process, CuO that was left after calcination is reduced to Cu (equation 4).



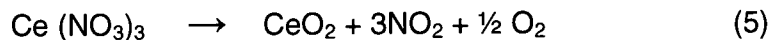
3.1.6 Preparation of CeO₂-Cu-YSZ cermet

a) Infiltration of Ce(NO₃)₃ and Cu(NO₃)₂

The samples were initially infiltrated with Ce(NO₃)₃ and calcined at 350°C for 30 minutes. Subsequently, these specimens were infiltrated with Cu(NO₃)₂ and calcined at 350°C for 30 minutes.

b) Calcination

During the process of calcination Cu(NO₃)₂ and Ce(NO₃)₃ were decomposed into CuO and CeO₂ according to the equations 3 and 5 respectively.



c) Reduction

After the completion of infiltration and subsequent calcination processes, the specimens were reduced in hydrogen atmosphere at 600 °C for 8 hours. During this process, CuO that was left after calcination is reduced to Cu and ceria remains the same. The specimens were thus left with CeO₂ and Cu.

3.2 Measurement of electrical properties

3.2.1 Resistance

In this experiment, a sinusoidal voltage is applied to a cell and the resulting current emerging from the cell is measured. The A.C current depends on two parameters. The first one is the ratio of the voltage and current and the second is the parameter ϕ which is the phase difference between the voltage and current. The combination of these two represents the impedance (Z) and is expressed in terms of an impedance magnitude Z_o and a phase shift ϕ as equation 6.

$$Z = Z_o(\cos\phi + j \sin\phi) \quad (6)$$

where $Z_{\text{real}} = Z_o \cos\phi$ and $Z_{\text{imag}} = Z_o j \sin\phi$. The impedance is also a function of frequency of the applied voltage. Generally, it is measured at a wide range of frequencies and plotted in terms of real and imaginary components of impedance (Z_{real} on the x-axis and $-Z_{\text{imag}}$ on the y-axis). Such graphical representations of impedance data are known as Nyquist plots. A Nyquist plot generally summarizes the impedance behavior of a system over many orders of frequency.

For measuring the impedance of a specimen a Solarton 1260 impedance/gain phase analyzer with 1287 electrochemical interface was used in the frequency range of 0.01 Hz to 100 KHz. The analyzer is designed to measure impedance and phase angle by software called Z-view provided by the manufacturer.

A typical Nyquist plot of a specimen is shown in Figure 3.2 R_1 is interpreted as the contact resistance and varies from specimen to specimen.

Difference of R_2 and R_1 is resistance R of the specimen and used in calculating conductivity of the specimen.

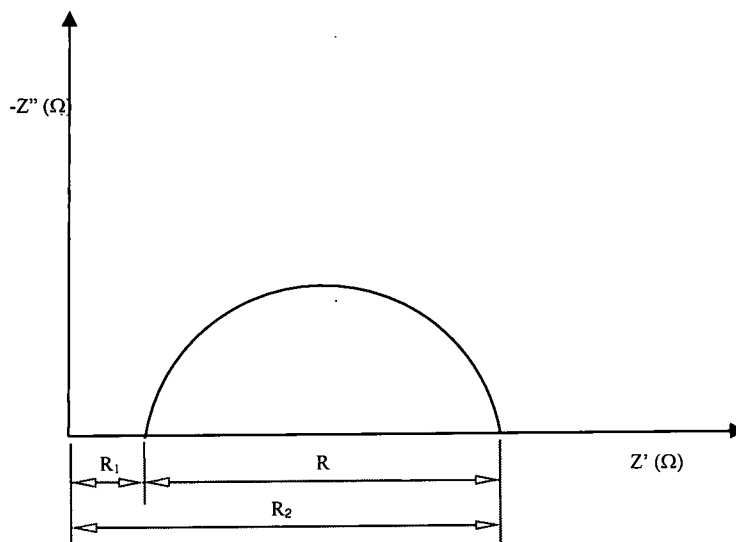


Figure 3.2: Nyquist plot of a typical specimen

3.2.2 Conductivity

Conductivity of specimens is calculated using the equation 7.

$$\sigma = \frac{t}{A} \left(\frac{1}{R} \right) \quad (7)$$

Where t = thickness of the sample,

A = area of cross section,

R = resistance

3.2.3 Transport number

Cermets are mixed conductors i.e. it conducts both oxygen ions and electrons. The measured conductivity is sum of the conductivities of ions and electrons. Contribution of each species can be expressed by transport number and can be determined by current relaxation method.

In current relaxation method the specimen is subjected to a d.c. voltage and current is monitored as a function of time. The initial decay in current is attributed to ionic conductivity (σ_i) and the steady state current (I_s) is related to the electronic conductivity. The data available from this graph allows one to calculate ionic (t_i^+) and electronic (t_e^-) transport numbers using the following equations:

$$t_i^+ = \frac{I_o - I_s}{I_o} \quad (8)$$

$$t_e^- = \frac{I_s}{I_o} \quad (9)$$

where I_o = the current at $t = 0$ and I_s = steady state current.

3.2.4 Activation energy

Relationship between conductivity and activation energy is given by the equation called Arrhenius equation and is expressed as

$$\sigma = -Ae^{\frac{-E_a}{RT}} \quad (10)$$

where, σ = conductivity

A = pre-exponential factor

E_a = activation energy

T = Temperature (K)

R = Gas constant.

Taking natural logarithm of above equation yields,

$$\ln(\sigma) = \frac{-E_a}{R} \left(\frac{1}{T} \right) + \ln(A) \quad (11)$$

and this is of the form $y = mx + b$, where,

$$y = \ln(\sigma)$$

$$m = -E_a / R$$

$$x = 1 / T$$

$$b = \ln(A).$$

A plot drawn between conductivity and temperature ($1/T$ on x-axis and $\ln(\sigma)$ on y-axis) yields a straight line. Multiplying slope of the line with R gives activation energy, E_a .

3.3 Preparation of YSZ bi-layer tape

Slurries required to make dense and porous YSZ tapes were prepared as discussed in section 3.1.1 and 3.1.3. First dense layer was tape cast using doctor blade on a Mylar sheet. After 5 hours, porous layer was cast on top of the dense layer. This bi-layer was left at room temperature for 3 days for drying. The bi-layer YSZ tape thus obtained was also flexible and can be cut into desired geometry. Specimens of desired geometry were cut and subjected to binder burnout and sintering processes. For a typical binder burnout a slow heating rate of $0.5\text{ }^{\circ}\text{C min}^{-1}$ from 25 to $500\text{ }^{\circ}\text{C}$ was practiced to avoid warping and pin holes. The heating rate was increased to $1^{\circ}\text{C min}^{-1}$ from 500 to $1350\text{ }^{\circ}\text{C}$ and soaked at this temperature for 2 hours. It was cooled down to room temperature at the rate of $3\text{ }^{\circ}\text{C per minute}$. Thereafter, sintering was carried out by ramping up at the rate of $1\text{ }^{\circ}\text{C per minute}$ to $1550\text{ }^{\circ}\text{C}$. After sintering at this temperature for 2 hours, it was cooled down to room temperature at the rate of $3\text{ }^{\circ}\text{C per minute}$.

3.4 Preparation of a SOFC

Presence of interlayer between electrolyte and cathode decreases the resistance of the cell. Therefore, after metal was impregnated into the porous side of bi-layer YSZ specimens to function as an anode, an interlayer was applied on electrolyte side before cathode layer was applied.

The interlayer composition constituted of YSZ and LSM powders which were mixed in equal proportions. A paste was prepared by adding xylene and alcohol to the mixture. Thin layer of this paste was applied on the dense side of bi-layer and subjected to sintering temperature of 1200 °C which was arrived by using a heating rate of 2 °C /min. This thin layer acted as interlayer between electrolyte and cathode.

Over the interlayer, a cathode layer constituting of LSM powder, xylene and alcohol was applied. The specimens thus prepared were subjected to a sintering at 1200 °C. The heating rate up to 1200 °C was 2 °C/minute.

The cells were initially coated with platinum paste and fired at 980°C for 30 minutes. After application of the platinum paste and subsequent firings, the anode and cathode sides for the four specimens were photographed and are shown in Figure 3.3. Platinum lead wires were attached to the platinized electrodes. Figure 3.4 shows photographs of the anode and cathode sides before and after firing at 980°C for 30 minutes. After attachment of the platinum lead wires, the cell was cemented to the side of a ceramic tube. The other side of the ceramic tube was connected with tubes for the fuel inlet and outlet. Photographs of the ceramic tube with the attached cell and fuel inlet/outlet are shown in Figure 3.5.

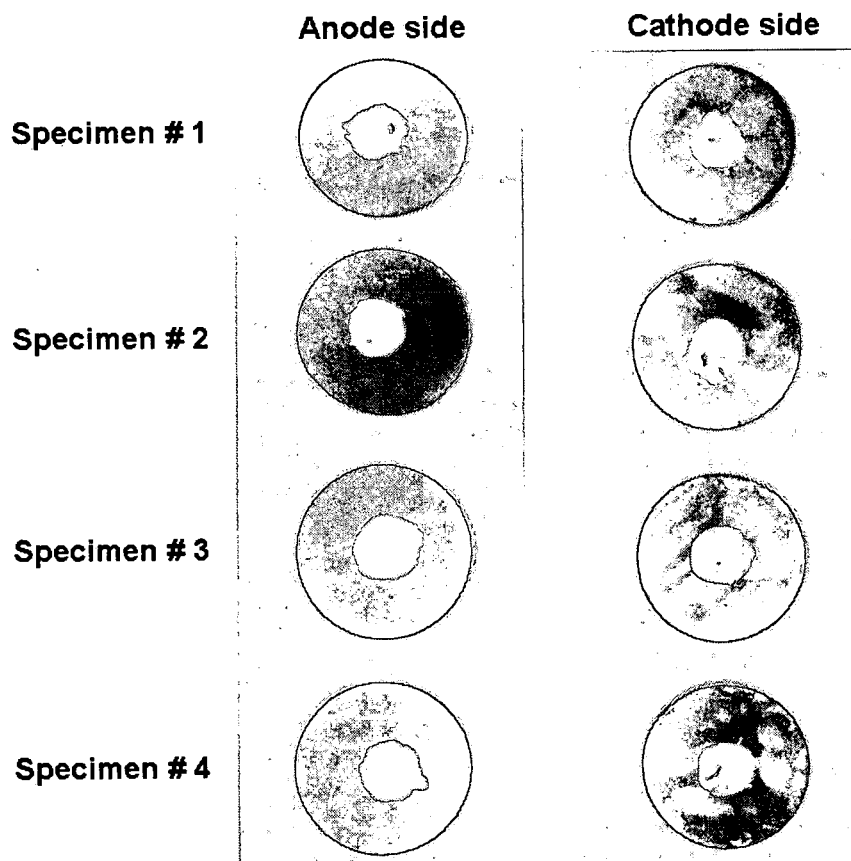


Figure 3.3: Anode and cathode sides of the four specimens after firing at 980°C for 30 minutes.

Thus, SOFCs were made for performance test. For this platinum leads were applied on both sides of the SOFC. Then, these SOFCs were mounted on a test fixture.

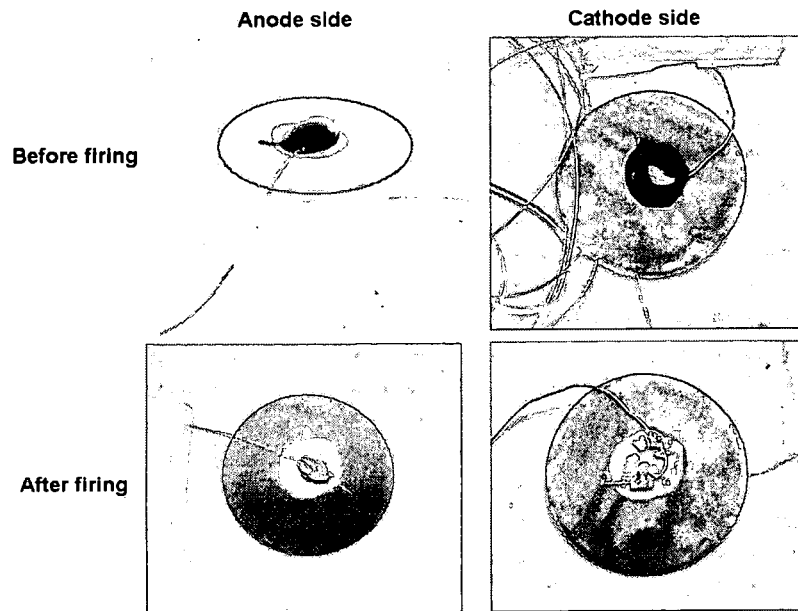


Figure 3.4: Platinum lead wire attachments to the platinized surface on electrodes before and after firing for 980°C for 30 minutes.

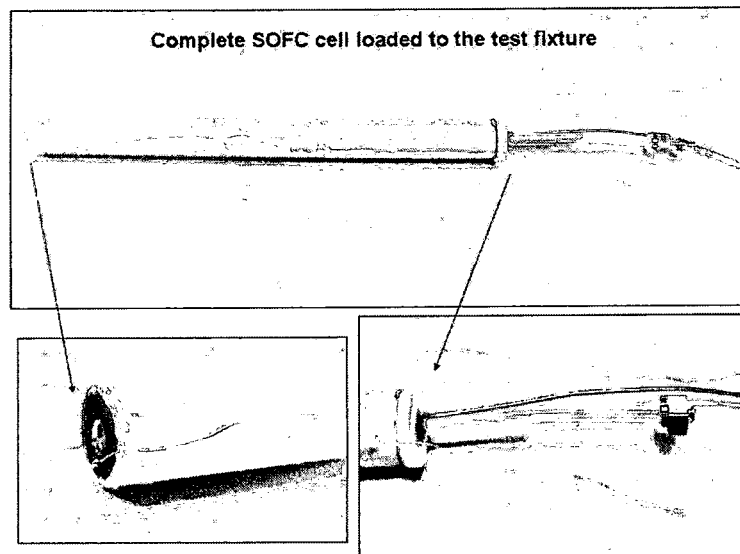


Figure 3.5: SOFC cell cemented onto a ceramic tube with fuel inlet and outlet tubes.

CHAPTER IV

RESULTS AND DISCUSSION

SOFC is a multifunctional, complex structure. It conducts and facilitates several electrical and electrochemical processes during its operation in a wide temperature range. In order to fabricate a functional SOFC, an extensive processing and characterization efforts are required. This section of the thesis presents details of processing and characterization techniques such as preparation of porous YSZ layer using rice flour and graphite as pore formers, microstructure characterization of sintered YSZ by porosity measurement and scanning electron microscopy, infiltration of the porous structure with Cu and CeO₂, electrical conductivity measurements of single and bi-layer YSZ and finally evaluation of a complete SOFC in hydrogen atmosphere.

4.1 Electrical conductivity measurement of single porous YSZ and YSZ - Ni layers

Initially rice flour was used as a pore former (commonly used in ceramic processing) in YSZ in an attempt to make porous anodic structure with Ni. This subsection presents a relative comparison of electrical properties of YSZ and YSZ-Ni porous structures.

Single layer porous YSZ having a porosity of 149.24 % was impregnated with 5.0 molar Ni(NO₃)₂ solution, calcined and reduced as

discussed in previous section. The specimen was characterized by impedance measurements. Figures 4.1 and 4.2 shows the impedance spectra of porous YSZ and Ni-YSZ membrane with 21 wt% of Ni in the temperature range of 600 to 850°C. The impedance spectra of Figure 4.1 are typical of porous YSZ material comprising of distorted semicircles. The intersections of these semicircles with the real axis (z') lead to the determination of resistance of the membrane. The shape of the impedance spectra has changed significantly after the introduction of nickel, Figure 4.2. The resistances of two specimens at different temperatures are presented in Table 4.1. From the table it can be noted that the resistance of porous YSZ decreases with increase in temperature, which is typical of ionic conduction mechanism. Similarly, for Ni-YSZ cermet the resistance is decreasing with increasing temperature. Even in the presence of Ni, the ionic conduction mechanism is the dominating factor. At lower temperature (600 °C), the presence of Ni decreased the resistance of Ni-YSZ by a factor of 10 when compared to the porous YSZ. However, at higher temperature the resistances are comparable. The Arrhenius plots of the conductivity data of porous YSZ and Ni-YSZ cermet specimens are presented in Figure 4.3.

The presence of Ni in YSZ should contribute to electronic transport and exhibit an increased resistance with increasing temperature. However, the YSZ-Ni cermet shows the reverse trend which implies discontinuity of Ni in the cermet. This discontinuity of Ni is because of pore geometry and its connectivity in the cermet. This observation is linked to the use of rice flour as the pore former. So from here onwards instead of the rice flour another

pore former, graphite is used for processing YSZ layer for fabricating anodic structure.

Table.4.1: Resistances of specimens at temperature ranging from 600 to 850 °C.

YSZ		Ni-YSZ	
Temperature (°C)	Resistance (Ω)	Temperature (°C)	Resistance (Ω)
600	724.00	607	70.51
650	196.50	657	33.90
700	041.46	706	15.48
750	013.01	754	07.65
800	004.92	803	04.03
850	002.21	851	02.94

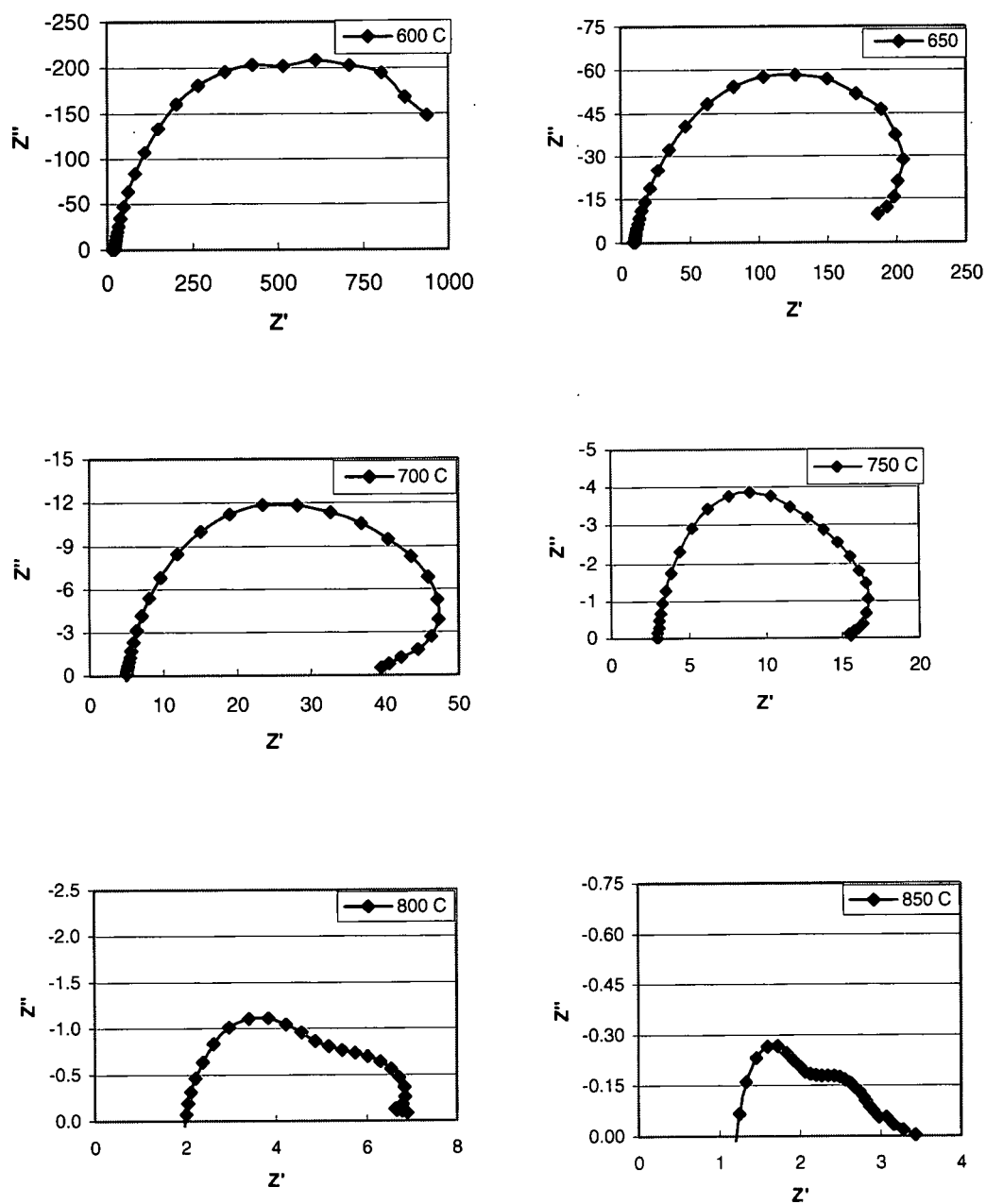


Figure 4.1: Impedance spectra of porous YSZ at 600, 650, 700, 750, 800 and 850 °C

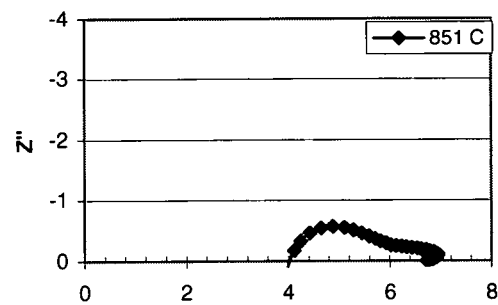
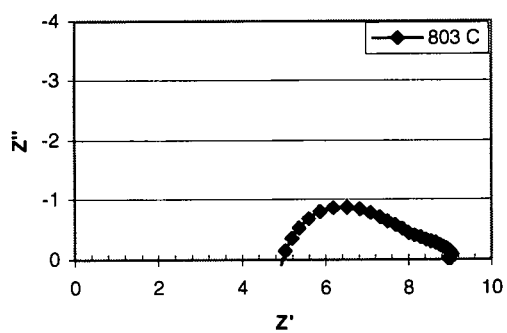
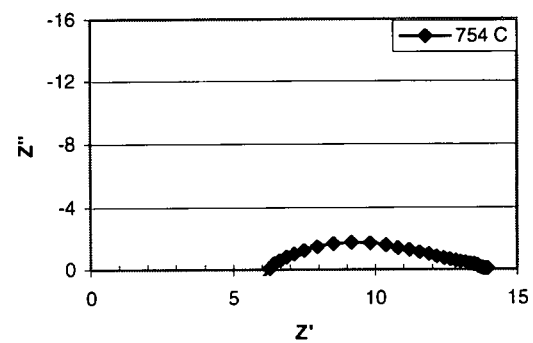
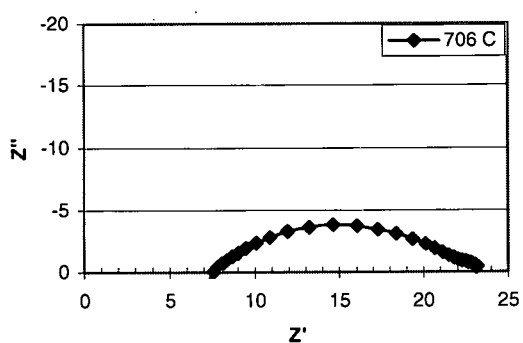
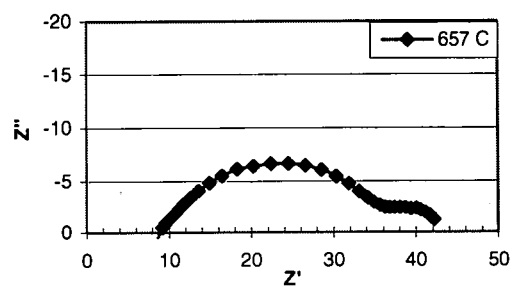
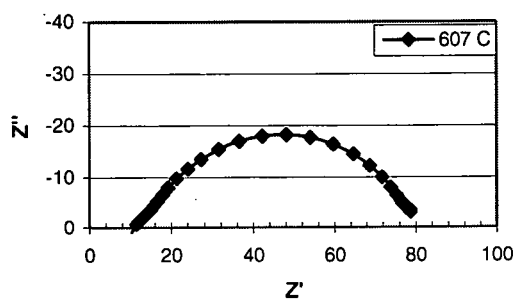


Figure 4.2: Impedance spectra of porous YSZ-Ni cermet at 607, 657, 706, 754, 803 and 851 °C

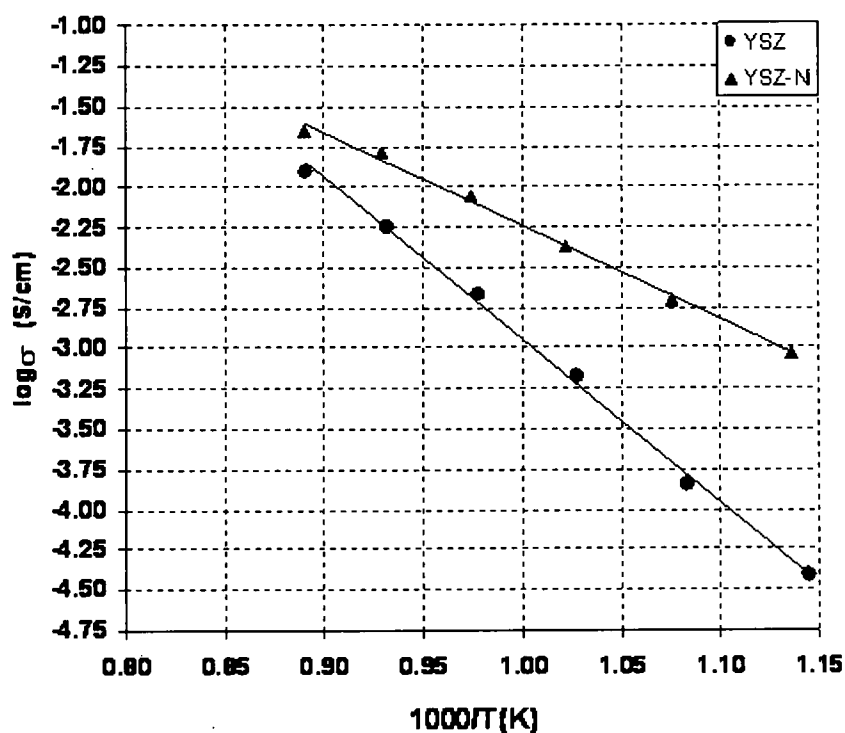


Figure 4.3: Arrhenius plots of porous YSZ and Ni-YSZ cermet specimens from 600 to 850 °C.

4.2 Conductivity of anodic membranes using graphite pore former

A green tape of YSZ was prepared using 45 wt% of graphite pore former (particle size 325 mesh). Then it was sintered at 1400°C for 4 hours. Measured porosity of the specimens was 111.76%. These specimens were soaked in 6.02 M nickel nitrate ($\text{Ni}(\text{NO}_3)_2$) solution. The physical appearances of the YSZ porous disc, $\text{Ni}(\text{NO}_3)_2$ infiltrated and calcined at 500°C, and YSZ-Ni cermet obtained after sintering at 1400 °C for 2 hours are shown in Figure 4.4.

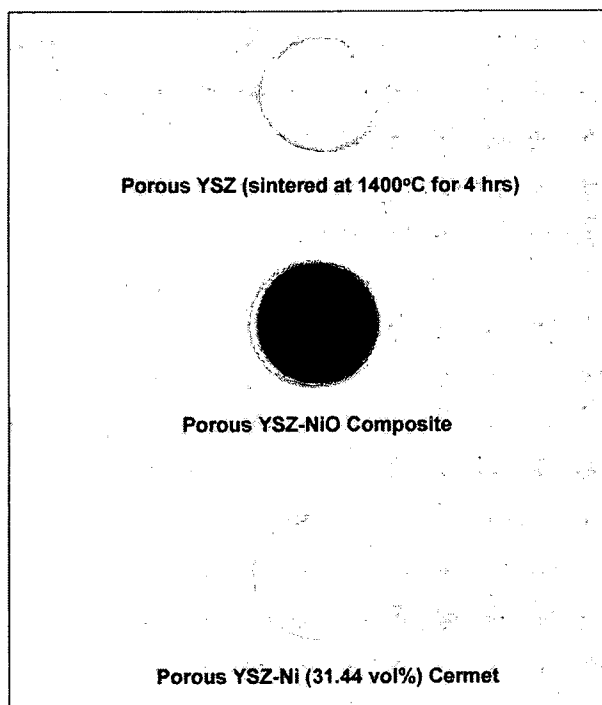


Figure 4.4: Photographs of porous YSZ, YSZ-NiO composite, and YSZ-Ni cermet.

The resistance of YSZ-Ni cermet specimen as determined by a multimeter was about 0.2Ω . The porosity of the specimens as measured by the water saturation technique after the infiltration of $\text{Ni}(\text{NO}_3)_2$, calcination at 500°C and sintering at 1400°C for 2 hrs was 48%. Therefore, the cermet is composed of YSZ (36.4 vol %), Ni (15.6 vol %) and porosity (48 vol %).

The YSZ-Ni cermet was also characterized by the AC impedance technique. The AC impedance data are shown in Figure 4.5. The intercept at real axis (z') is equal to 0.16Ω which matches closely with the resistance measured by the multimeter.

The YSZ-Ni cermet specimen was subjected to a bias d.c voltage of 40 mV and current was monitored as a function of time. The current vs. time plot is shown in Figure 4.6. The data of Figure 4.6 allows one to calculate ionic

(t_i^+) and electronic (t_e^-) transport numbers using the equations 3 and 4 of section 3.2.3.

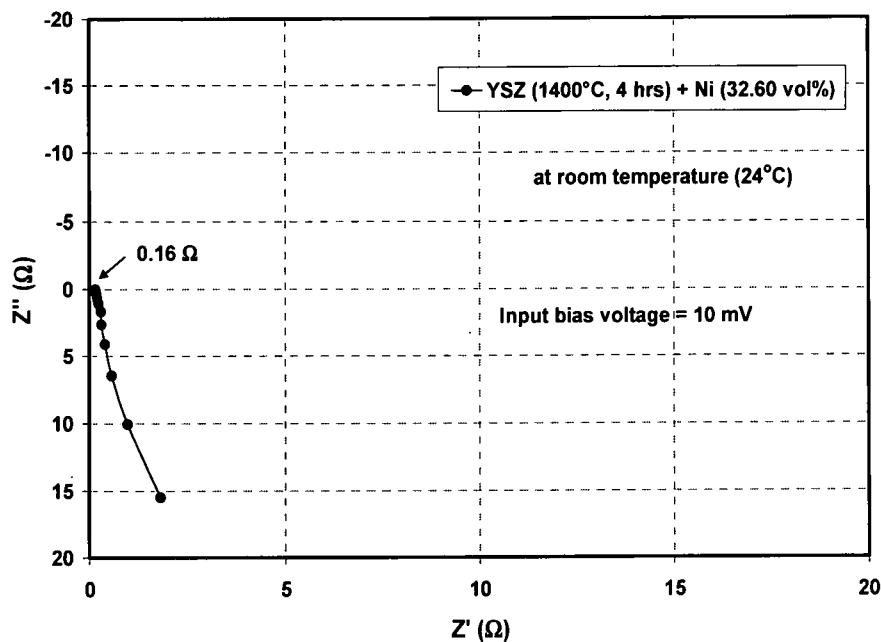


Figure 4.5: Complex impedance plot of YSZ-Ni cermet at room temperature (24°C).

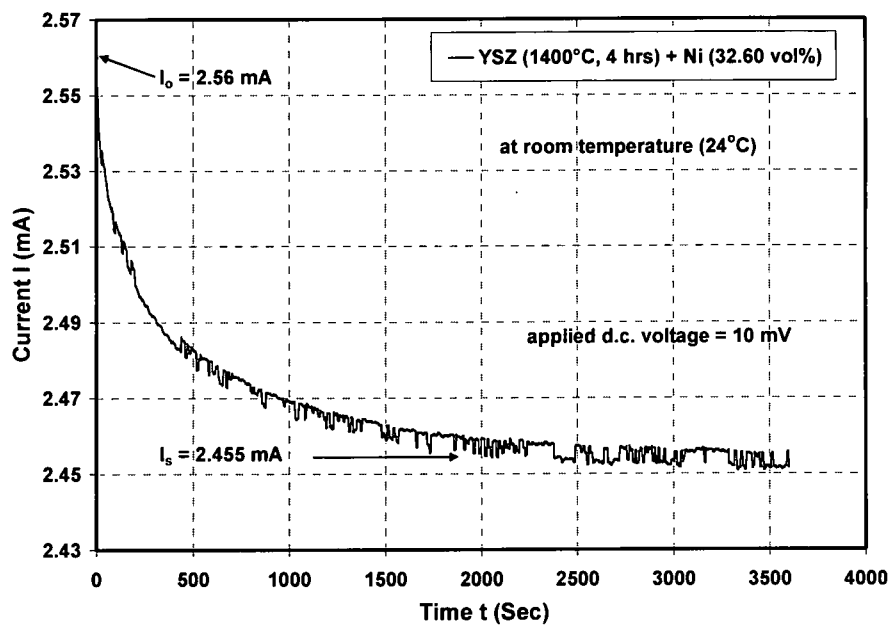


Figure 4.6: Current versus time plot of YSZ-Ni cermet at room temperature (24°C).

The ionic transport (t_i^+) and electronic transport numbers (t_e^-) were determined to be 0.04 and 0.96. Therefore, the YSZ-Ni cermet in spite of the fact that it contains only 15.6 vol% of Ni is primarily an electronic conductor at room temperature.

In section 4.1, it was stated that the resistance of the YSZ-Ni cermet that was prepared using the rice flour was around $2\ \Omega$ at $850\ ^\circ\text{C}$ whereas the resistance of YSZ-Ni cermet that is prepared using graphite as pore former is only $0.16\ \Omega$ at room temperature. This decrease in the electrical resistance of the specimen was possible because of better connectivity of Ni metal and higher porosity of the specimen which in turn was due to the usage of graphite as pore former. This result conclusively narrowed the choice of pore former in favor of graphite powder.

4.3 Electrical conductivity of the porous YSZ - Cu cermet

It has been indicated earlier that Ni (a widely used anodic component of SOFC) is not stable in contact with hydrocarbon fuels. Therefore, Ni needed to be replaced with other metal and Cu was determined to be a suitable choice.

Porous YSZ specimens were soaked in 5.08 M copper nitrate solution and calcined at $350\ ^\circ\text{C}$ for 30 minutes. The specimens were soaked and calcined for a number of times to obtain YSZ-Cu cermet specimens containing 4.31, 5.89, 7.88 and 9.84 vol% of Cu after reducing the calcined samples at $600\ ^\circ\text{C}$ for 8 hours in hydrogen atmosphere. The AC impedance measurements on these specimens were conducted in the temperature range of -60 to 25°C . The conductivity data as obtained from the AC measurements

are shown in Figure 4.7. The temperature dependence data shows a typical behavior of semiconductors. In spite of the presence of copper in these specimens, an absence of metallic behavior is noted.

The conductivity increases initially as the Cu concentration increases from 4.31 to 5.89 vol%. Subsequent increase in copper concentration led to a decrease in the conductivity. The specimens were again reduced at 600 °C for the second time and conductivity measurement was conducted.

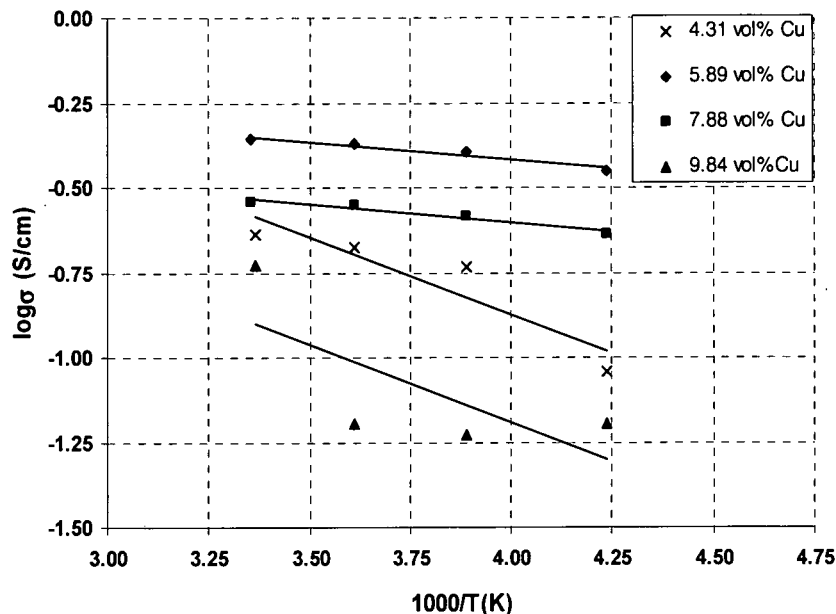


Figure 4.7: Temperature dependence of conductivity of Cu-YSZ cermets containing 4.31, 5.89, 7.88 and 9.84 vol% of Cu after 1st time reduction.

The data from these measurements are shown in Fig. 4.8. The data shows that there is a better fit of the measured value with the linear Arrhenius plots. However, there is a change of about 45% in the conductivity values after second reduction. The nature of the change is depicted in Figure 4.9. The

variation in conductivity from the first reduction to second reduction ranges from 30 to 60%. The variation is attributed to structural changes that took place between the first and second reductions. The data also suggests that copper concentration over 5.89 vol% is detrimental to electrical conductivity. From the Figure 4.9 it can be inferred that the conductivity of the specimen increases initially with an increase in the concentration of copper from 4.31 to 5.89. With further increase in the concentration of copper, the conductivity decreases. The maximum conductivity was obtained at 5.89 vol% of copper.

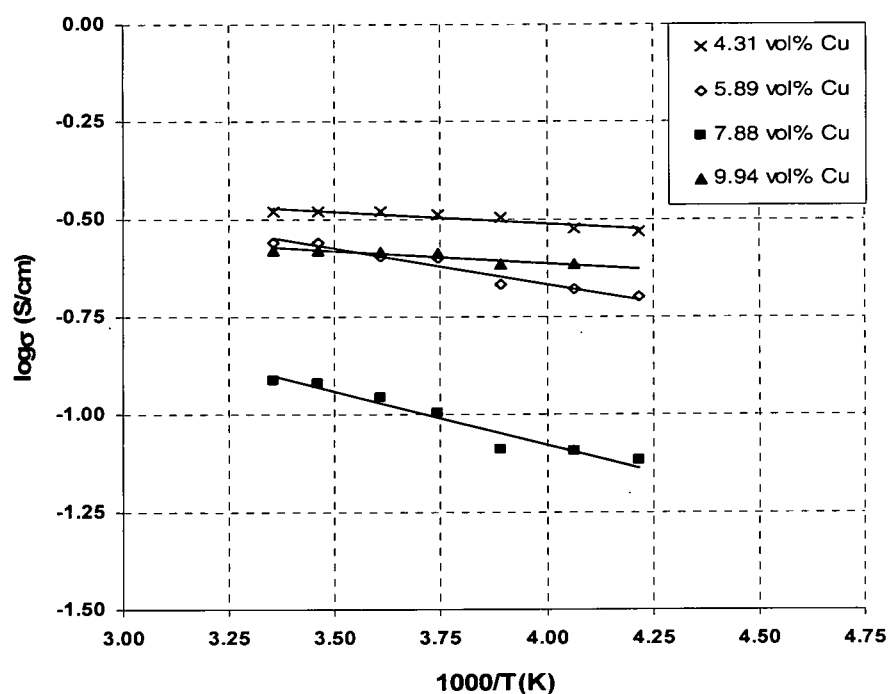


Figure 4.8: Temperature dependence of conductivity of Cu-YSZ cermets containing 4.31, 5.89, 7.88 and 9.84 vol% of Cu after 2nd reduction.

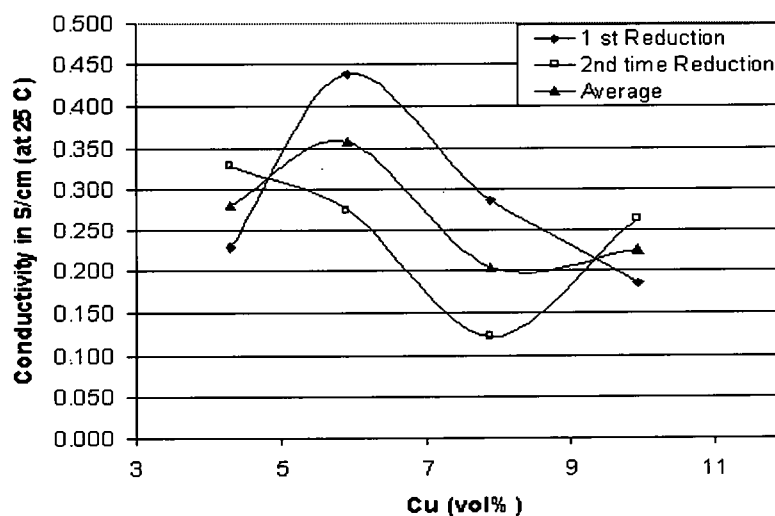


Figure 4.9: Conductivity of Cu-YSZ cermet as a function of vol% of Cu at 25°C.

The electronic transport number, t_e^- of all the YSZ-Cu cermet specimens was measured using the current relaxation method after application of 40 mV of DC potential. The electronic transport number data as a function of copper concentration are shown in Figure 4.10.

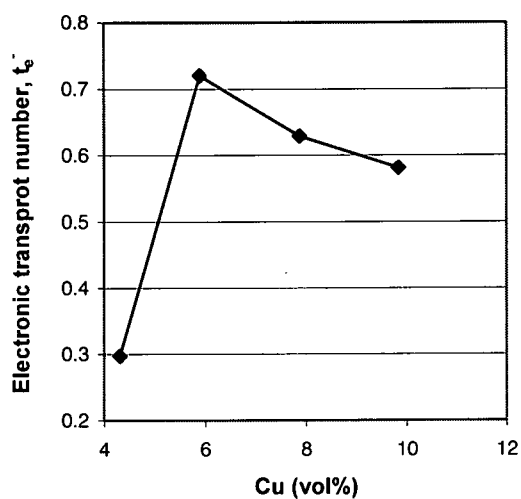


Figure 4.10: The electronic transport number of YSZ-Cu cermet as a function of copper concentration.

The electronic transport number, t_e^- , increases from 0.3 to 0.72 as the volume percent of Cu increases from 4.31 to 5.89. Further increase in Cu concentration led to a decrease in t_e^- to 0.63 and 0.58 for 7.88 and 9.94 vol% Cu, respectively. The decrease in electronic transport number is attributed to agglomeration of Cu particles at higher concentrations of copper. The electronic transport number basically follows the trend of the conductivity data as presented in Figure 4.9.

4.4 Electrical conductivity of the porous YSZ – Cu/CeO₂ cermet

It was indicated earlier that copper can only conduct electrons in the cermet but has no catalytic activity to oxidize the fuel. This problem can be overcome by adding one more material to the cermet which has good catalytic activity and ceria (CeO₂) is the choice.

Several porous YSZ specimens (porosity ~70%) were initially infiltrated with cerium nitrate solution (Ce(NO₃)₂) and calcined at 350°C for 30 minutes. Subsequently, these specimens were infiltrated with copper nitrate solution (Cu(NO₃)₂) and calcined at 350°C for 30 minutes. The goal of the Cu(NO₃)₂ infiltration was to achieve 5.9 vol% of copper (20 wt%) after reduction of CuO to Cu in hydrogen atmosphere at 650°C for 8 hours. The specimens thus prepared were characterized for electrical properties. Table 4.2 presents the relative volume percent composition of the specimens. It can be noted from the Table 4.2 that the major variable is the concentration of CeO₂ in volume percent. Other constituents of the anode, such as YSZ, Cu, and porosity remain relatively constant.

Table 4.2: Volume Percent Composition of the Cu/CeO₂-YSZ Anode Specimens

Specimen	YSZ	CeO ₂	Cu	Porosity	Activation Energy (eV)
1	23.00	0	5.90	72.10	0.021
2	23.00	2.56	6.75	67.69	0.185
3	23.00	5.12	7.70	64.10	0.053
4	23.00	7.39	8.26	61.35	0.011

The Arrhenius plots of the conductivity data of the YSZ – Cu/CeO₂ specimens are presented in Figure 4.11. The introduction of CeO₂ in the porous structure decreases the conductivity of the cermet initially. However, the conductivity increases as the concentration of CeO₂ in the specimens was further increased. It can also be noted from the figure 4.11 that even after the introduction of 7.39 vol% of CeO₂, the conductivity of the YSZ - Cu/CeO₂ cermet remains lower than the conductivity of YSZ - Cu cermet containing 5.90 vol% of copper. This suggests that the introduction of CeO₂ to the Cu-YSZ specimen disrupted continuity of the copper and apparently a mixing of CeO₂ and Cu has taken place. This scenario is beneficial from the catalysis point of view. The activation energy for conduction of these specimens is also presented in Table 4.2. The activation energy varies from 0.011 to 0.185 eV, signifying a semiconductor type of conduction behavior around room temperature.

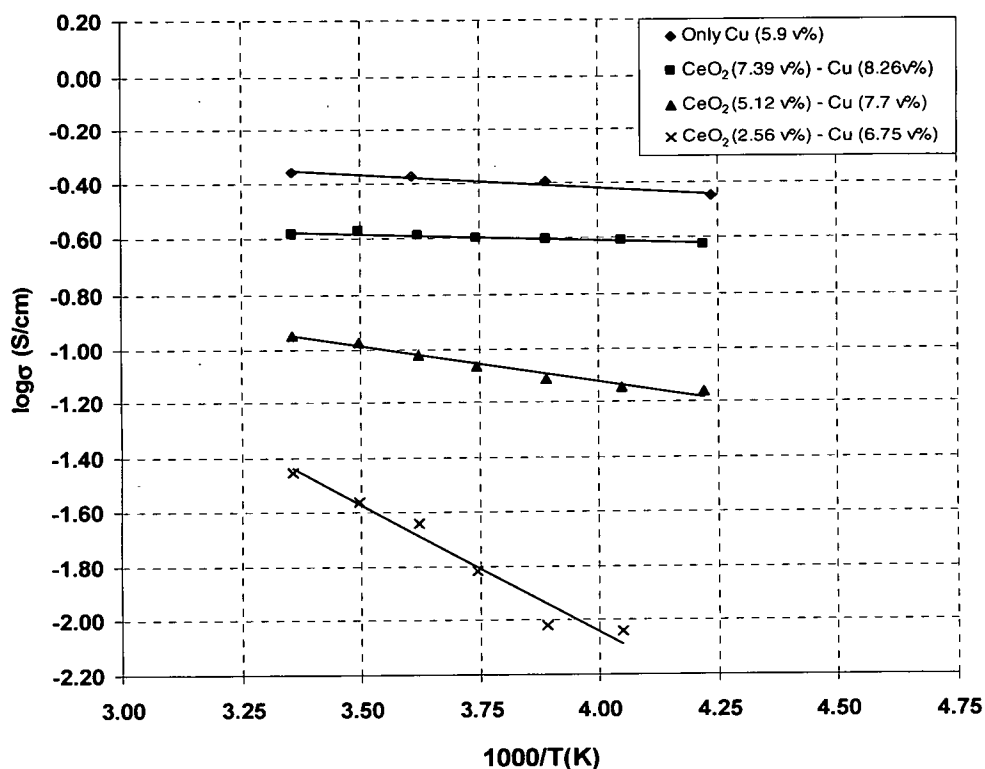


Figure 4.11: Arrhenius plots of YSZ – Cu/CeO₂ anodic specimens from -35 to 25 °C.

The conductivities of the YSZ - Cu/CeO₂ specimens as a function of CeO₂ concentration at room temperature are presented in Figure 4.12. The conductivity increases from about 35 mS cm⁻¹ for 2.56 vol% CeO₂ to 262 mS cm⁻¹ for 7.39 vol% of CeO₂. It is believed that a seven-fold increase in conductivity of the specimen should enable the material to perform satisfactorily as a direct oxidation anode. Hereafter, the porous YSZ with Cu and CeO₂ are referred as anode or anodic structure.

It is apparent that the cermet is a mixed conductor i.e. it conducts ions and electrons and conductivity exhibited by it is the sum of the conductivities

of ions and electrons. Therefore, it is necessary to quantify the contribution of individual species in the conduction process and this can be accomplished by measuring the electronic and ionic transport numbers of the specimen. As practiced earlier the specimens were subjected to a bias voltage of 10 mV followed by the measurement of current decay as a function of time.

From this measurement the steady state current and initial current are obtained. By substituting these values in equation 4 the electronic transport number is calculated. It should be noted that the sum of the transport numbers is always one. Therefore, the charged species with the highest transport number becomes the major contributor to the total conductivity of the cermet.

The electronic transport numbers of specimens containing various concentrations of CeO_2 are shown in Figure 4.13. It is apparent that the electronic transport number is more for the cermet with 5.12 vol% of CeO_2 and does not show any trend.

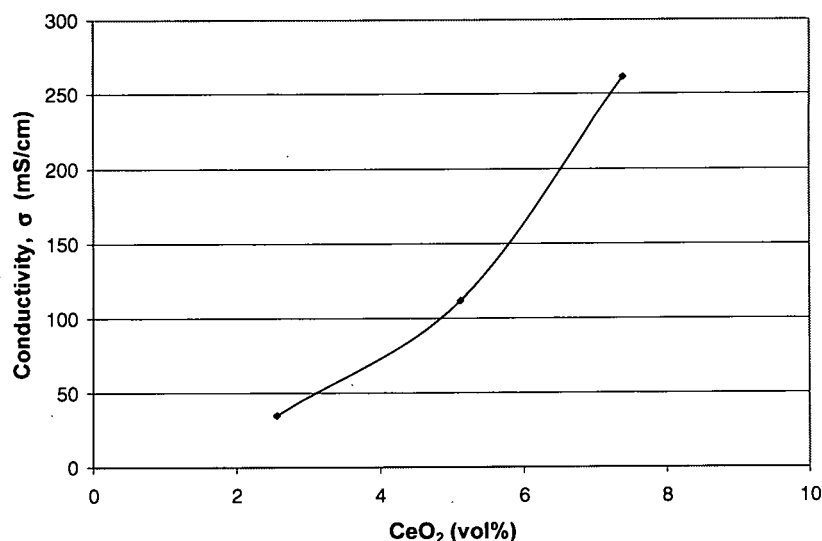


Figure 4.12: Conductivities of YSZ – Cu/ CeO_2 specimens as a function of CeO_2 concentration at room temperature

However, the specimen exhibit significant inhomogeneity with respect to electrical transport. Again, the mixed transport (ionic and electronic) should be useful for a high performance anode.

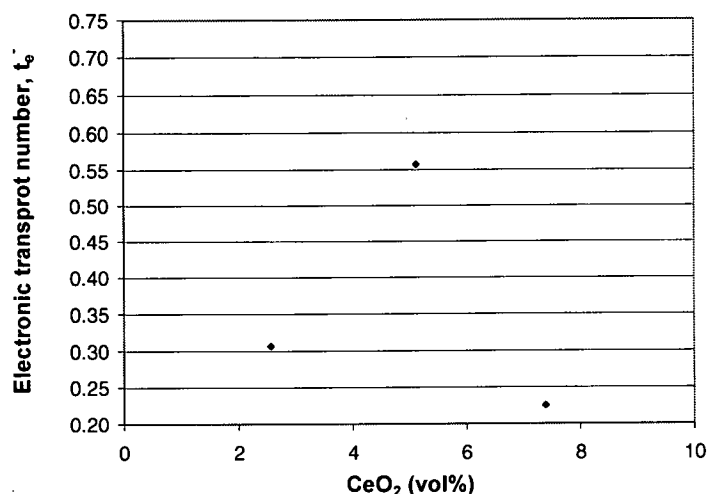


Figure 4.13: Electronic transport number, t_e^- of YSZ – Cu/CeO₂ specimens vs. CeO₂ concentration.

From the above observations it can be inferred that the total conductivity was higher for the cermet with 7.39 v% of CeO₂ but electronic transport number is higher for the cermet with 5.12 v% of CeO₂. It should also be noted that the electronic transport number of YSZ - Cu/CeO₂ specimens have significantly decreased as compared to the YSZ - Cu specimens (Fig. 4.10). The observations suggest that the CeO₂ addition has broken continuity of Cu within the porous structure and the CeO₂ is distributed in the entire structure which is beneficial for the electrochemical processes.

4.5 Micro-structural characterization of a YSZ – Cu/CeO₂ Anode

The scanning electron micrographs of a YSZ – Cu/CeO₂ anodic material containing 2.56 vol% CeO₂ and 6.75 vol% Cu are shown in Figure 4.14 which exhibits a microstructure containing a wide distribution of pores ranging in size from 1 to 24 μm . The cross-sectional width of the specimen is approximately 250 μm . The energy dispersive x-ray analysis was conducted from four different points located on the fractured cross section. It is apparent that Cu and CeO₂ concentrations vary considerably from one point to another and this can be seen in Table 4.3. It is also noted that both of the anodic constituents (Cu and CeO₂) have penetrated well within the interior of the specimen. In all likelihood, low Cu and CeO₂ concentrations reflect the location of the point in close proximity to the YSZ grains.

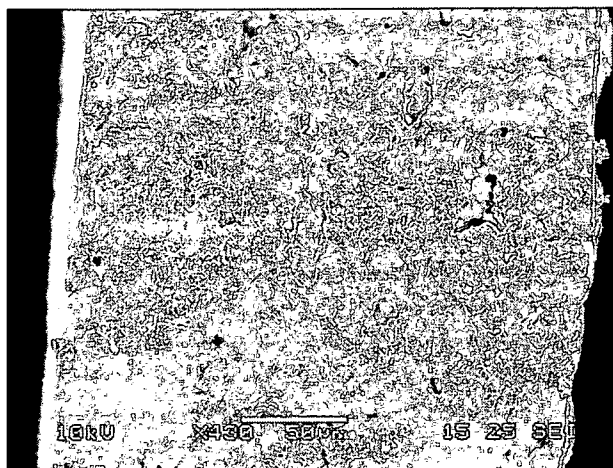


Figure 4.14: Scanning electron micrograph of a YSZ – Cu/CeO₂ anode.

Table 4.3: Atom concentration % at various points in the micrograph of

figure 4.14

Points	O	Cu	Zr	Ce
1	84.56	2.83		12.59
2	18.80	44.33	18.51	18.36
3	13.12	35.20	19.99	31.68
4	2.26	5.98	8.13	83.63

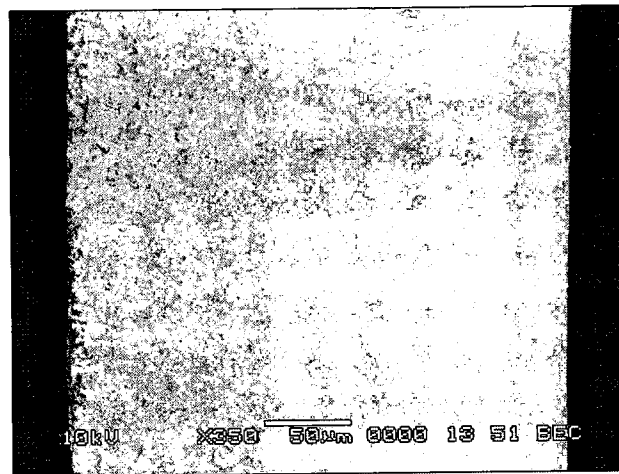
4.6 Characterization and optimization of bi-layer YSZ (porous and dense)

The next step towards processing of functional SOFC is the fabrication of bi-layers of YSZ in which the porous layer is modified to function as anode and the dense layer serves as membrane or electrolyte. The electrolyte layer needs to be totally dense so that the fuel or oxidant does not flow through it. Furthermore, the anodic layer after infiltration of Cu and CeO_2 should remain porous enough to accommodate fuels and catalyze the oxidation process in an efficient manner. In this section, experimental approaches and processing parameters leading to successful processing of bi-layers is presented.

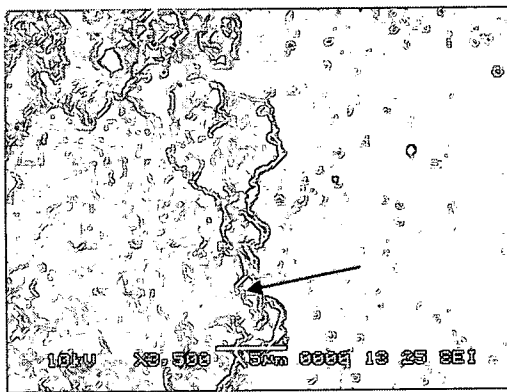
4.6.1 Optimization of sintering temperature and time

Bi-layer tapes prepared using the procedure discussed in section 3.3 were initially sintered at 1400°C for 4 hours. These specimens were characterized by SEM and Figure 4.15a shows the cross section of the bi-layer in which the left and right hand sides are porous and dense YSZ layers, respectively. The interface of the bi-layer in Figure 4.15b suggests continuity of YSZ between the two layers. The dense layer also shows isolated pores at

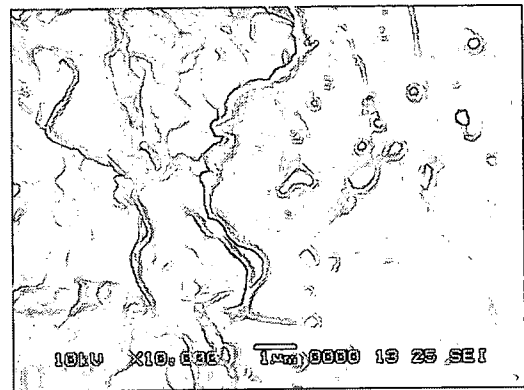
higher magnifications, Figure 4.15b. It is observed that the sintering parameters (temperature and time) are insufficient to fully densify the dense layer. At yet higher magnification, the interface shows similar features, Figure 4.15c. The isolated pores in the dense layer are approximately 500 nm in diameter.



(a)



(b)



(c)

Figure 4.15: SEM micrographs of the bi-layer interface at different magnifications. (a) X350, (b) X3,500 and (c) X10,000

The structure of the porous layer from the freshly fractured cross section of a bi-layer at higher magnification is shown in Figure 4.16a. This micrograph shows the existence of predominantly continuous pores; however, there are regions of isolated pores as indicated by an arrow. It should be

noted that the percent porosity as determined by the water saturation technique in this porous layer is about 40.4%. Figure 4.16b shows the surface of the cast porous layer. The existence of open pores is evident and permeation of anodic solution into the porous layer can be accomplished.

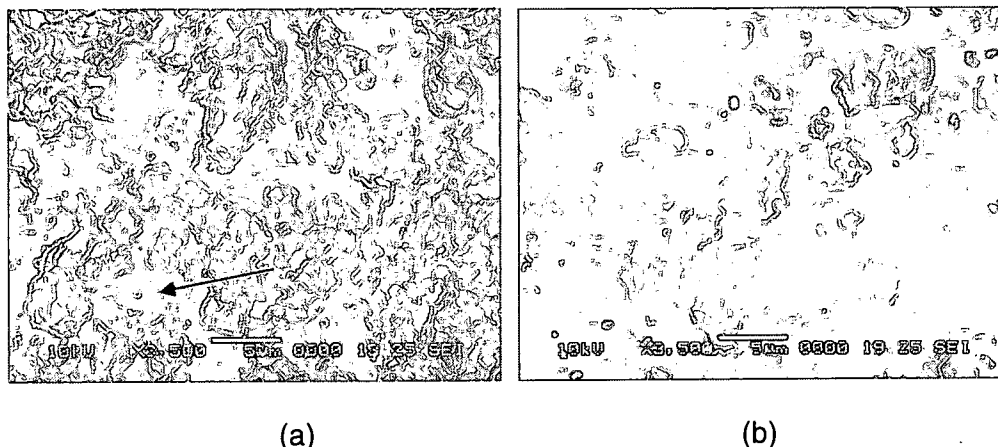


Figure 4.16: SEM micrographs of a) the cross section showing the porous layer b) the cast surface showing open pores on the porous surface.

In view of the partial sintering of dense layer by heat treatment at 1400 °C for 4 hrs, the specimen was subjected to additional heat treatment at 1500 °C for 1 hr for further densification. The morphology of the twice-sintered bi-layer specimen was evaluated using porosity measurements and scanning electron microscopy (SEM). The porosity of the porous layer was determined using the water saturation technique, whereas porosity of the dense layer was evaluated using SEM micrographs. The grain size variations of the two layers are shown in Figure 4.17. By increasing sintering temperature to 1500 °C, the grain size in both the layers increases. In the porous layer, YSZ grain size increased from 0.3 - 0.9 μm range to 0.5 - 1.5 μm range as the sintering temperature was raised to 1500°C. Similarly, the grain size of the dense layer increased from 1 - 2 μm range to 2 - 3 μm range with an increase in sintering temperature.

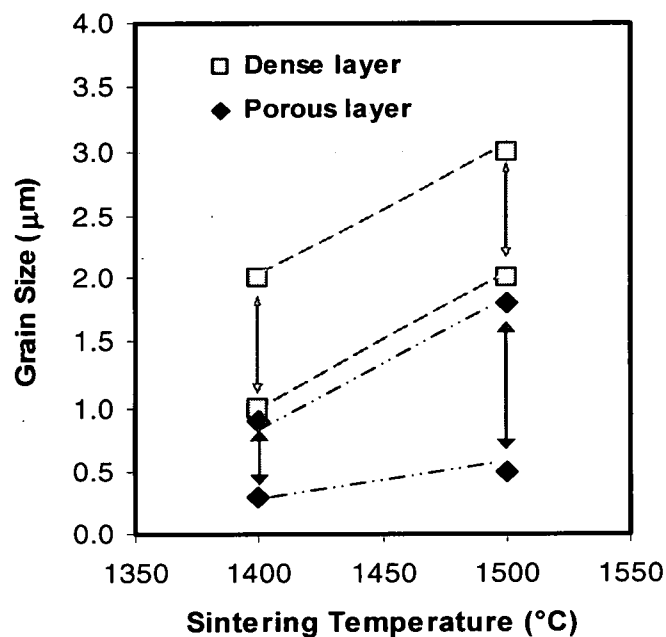
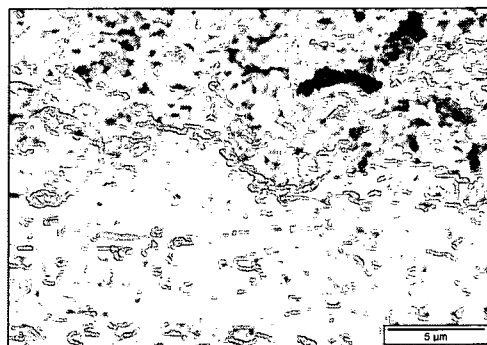
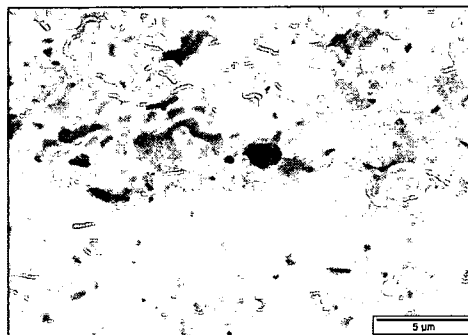


Figure 4.17: Grain size distribution in porous and dense layers of a bi-layer specimen sintered at 1400°C/4 hours and 1500°C/1 hour.

The SEM micrographs of the twice sintered bi-layers at high magnification is shown in Figures 4.18. The top layer is the porous layer and the bottom layer is the dense layer. The interface (Figure 4.18) of these layers is well diffused which should provide desirable electrochemical performance of the bi-layer. The grain size of the porous layer increased by additional



(a)



(b)

Figure 4.18: SEM micrographs of sintered bi-layer tape at higher resolution (3000 X)

(a) sintered at 1400 °C for 4 hrs, (b) sintered at 1400 °C for 4 hrs and 1500 °C for 1 hr

sintering at 1500°C while maintaining the continuity of pores. From these figures it is evident that dense layer still contained considerable number of closed pores.

The porosity of porous and dense layers decreased with increasing heat treatment temperature, as shown in Figure 4.19. The porous layer exhibits a porosity of 35% after sintering at 1500°C for 1 hour. The porosity is determined to be inadequate to provide space for the presence of catalyst and electronic conductor. The porosity of the dense layer, although small (3.5%), remained a matter of concern.

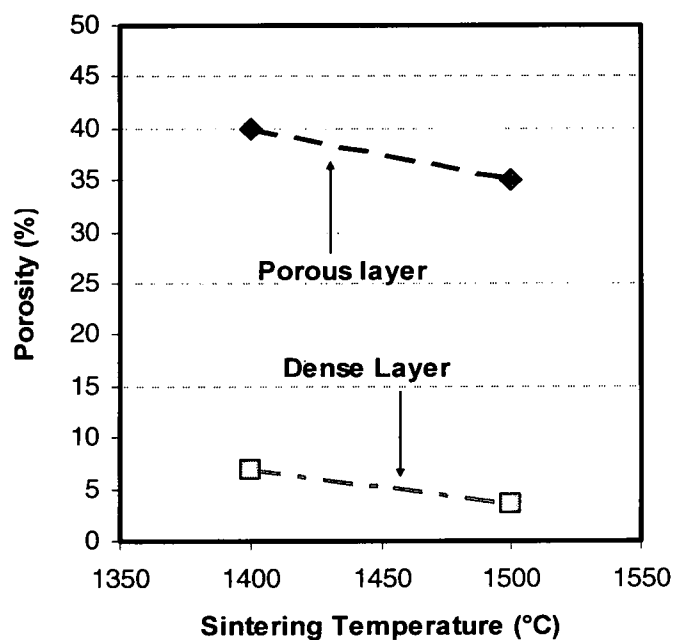


Figure 4.19: Porosity of porous and dense layers as a function of sintering temperature.

In view of the prior data on the effect of sintering temperature and time on YSZ grain size and porosity of both porous and dense layers, the sintering temperature and time were further increased to 1550 °C and 4 hrs

respectively. The SEM micrographs, Figure 4.20(a), revealed the presence of closed pores in the dense layer even after sintering at 1550 °C for 4 hrs. The estimated porosity of the dense layer is approximately 1.5%. This low porosity comprising of closed pores can be acceptable for fabricating a working SOFC cell. The high-resolution micrograph of the porous layer is shown in Figure 4.20(b). The porosity of porous layer also decreased which is not desirable.

The porosity versus sintering temperature of the dense layer specimens sintered at various temperatures is shown in Figure 4.21. It should be noted that sintering time at each temperature was different (1400 °C for 4 hrs, 1500 °C for 1 hr and 1550 °C for 4 hrs). It is apparent that increasing the sintering temperature reduced the porosity. The dense layer which was sintered at 1550 °C for 4 hours should adequately serve the purpose of an electrolyte. Therefore, the bi-layer specimens were sintered at 1550 °C for 4 hours for subsequent studies and it was recognized that the porosity of porous layer must be increased in order to accommodate the catalyst, electronic conductor (Cu) and fuel during operating conditions of the SOFC.

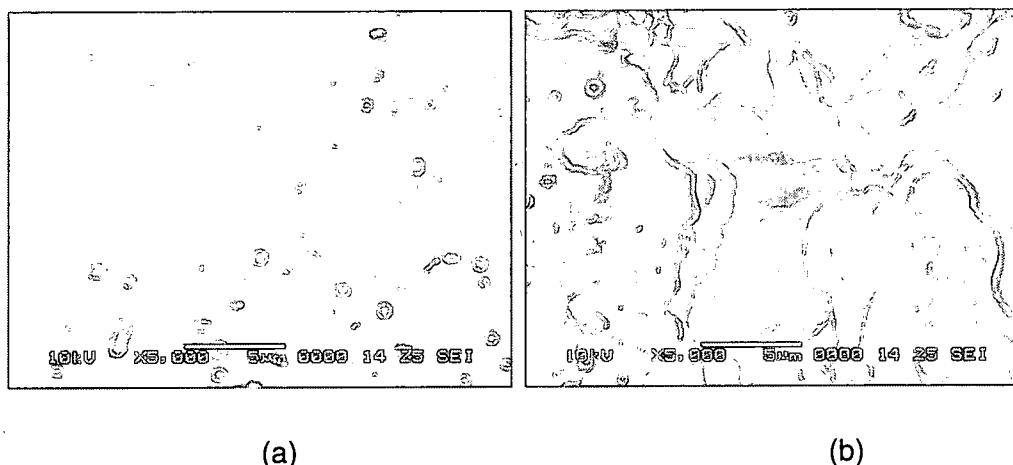


Figure 4.20: High resolution SEM micrographs of (a) dense layer and (b) porous layer. The bi-layer was sintered at 1550° for 4 hours.

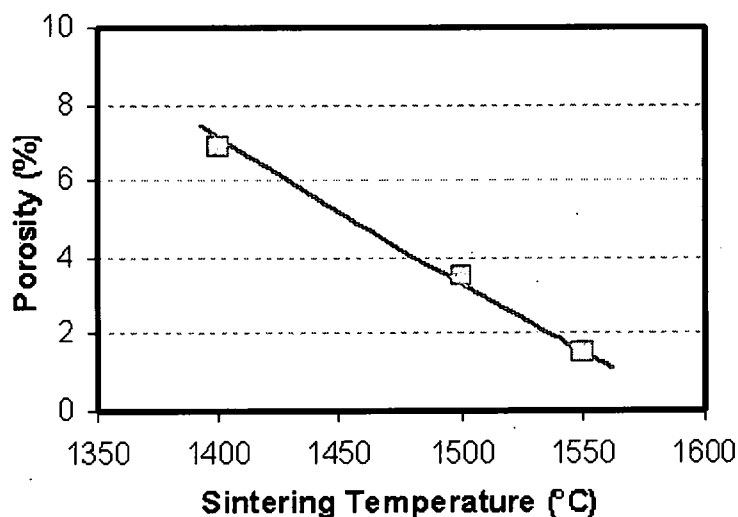


Figure 4.21: Porosity of the dense layer versus sintering temperature.

4.6.2 Optimization of graphite content in the porous layer

The sintering temperature of 1550 °C for 4 hrs of bi-layer specimens decreased the porosity of the porous layer to 35%. This is insufficient to introduce required amounts of anodic components (Cu and CeO₂). Therefore, porosity has to be increased using higher concentrations of graphite. In this section efforts related to optimization of graphite is presented.

The tape cast formulations using 0, 20, 30, 40, 45, 50 and 55 wt% of graphite were prepared and evaluated. The tapes were cast and dried without any cracks. Figure 4.22 shows a tape with 40 wt% graphite after drying. After sintering at 1550°C for 4 hrs, the specimens appeared smooth and uniform.

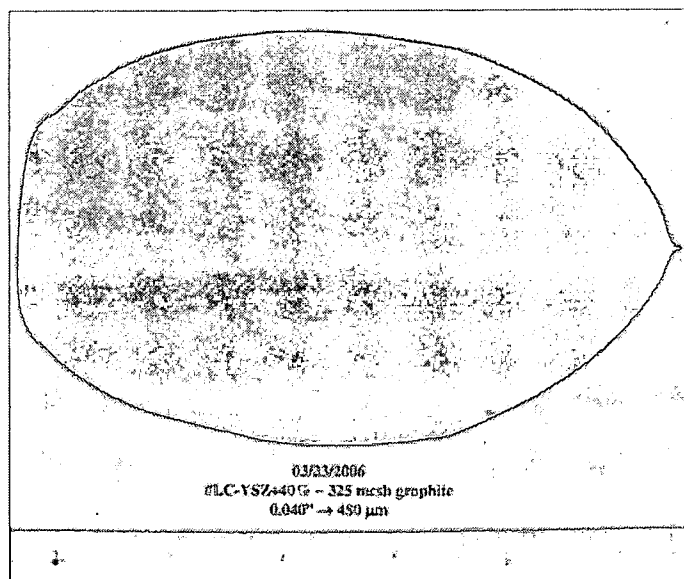


Figure 4.22: Dried tape with 40% graphite.

The porous tape was characterized for porosity and density, and the experimental data are shown in Figure 4.23 and Table 4.4. It should be noted that a porosity of 74.15 % can be obtained even after sintering at 1550°C. The experimental data of the present investigation is shown in Figure 4.23. It is apparent from the Figure 4.24 that the porosity increased significantly with an increase in wt% of graphite and remained constant for single porous layer for further increase in the graphite content. However, with bi-layer the porosity continues to increase as the graphite content is increased from 40 to 55 wt%. The specimens containing 50 and 55 wt% graphite were very fragile and disintegrated during the sintering process. From this study it is concluded that about 45 wt% graphite can be used safely, which can provide a mechanically strong bi-layer with the porous layer having a porosity of 64.15%.

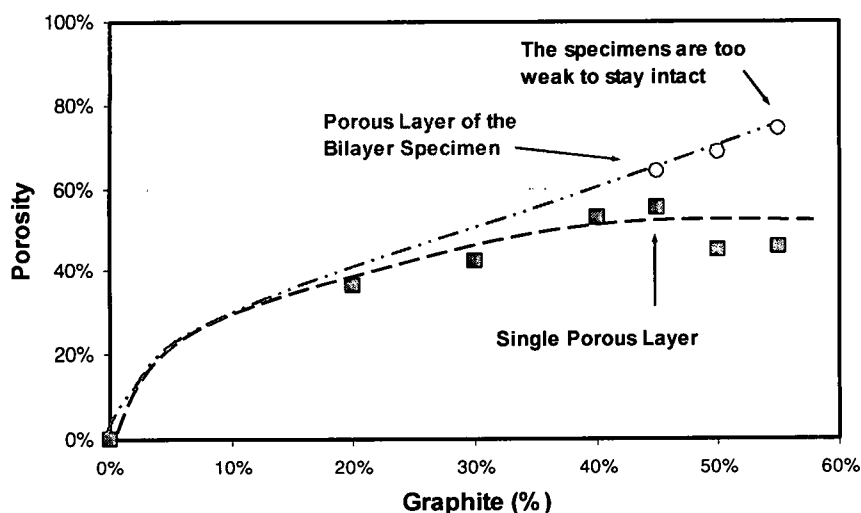


Figure 4.23 Porosity versus graphite content for single and bi-layers.

Table 4.4. Porosity and density after sintering at 1550°C for 4 hours.

Graphite (wt%)	0	20	30	40	45	50	55
Porosity (%)	0.00	36.35	42.59	53.02	64.15	68.64	74.15
Density (g/cm ³)	5.96	3.79	3.42	2.80	2.13	1.86	1.54

4.6.3 Optimizing the bi-layer processing

The tape casting for processing bi-layers was conducted in two steps. Initially, a thick layer of pure YSZ was cast with the doctor's blade setting at 0.01 inch. After drying the pure YSZ tape for 3 hours, a thick layer (0.045 inch) of YSZ-graphite slurry was cast. The surface of the bi-layer appeared uniform, as shown in Figure 4.24.

The green bi-layer tapes were sintered using two different sintering schedules. Figure 4.25 shows the appearance of the single and bi-layer specimens. In Figure 4.25 and row A, the single layer specimens are shown.

The bi-layer specimens which were sintered at 1550°C for 4 hours are shown in Row B. These specimens are warped and appear concave.

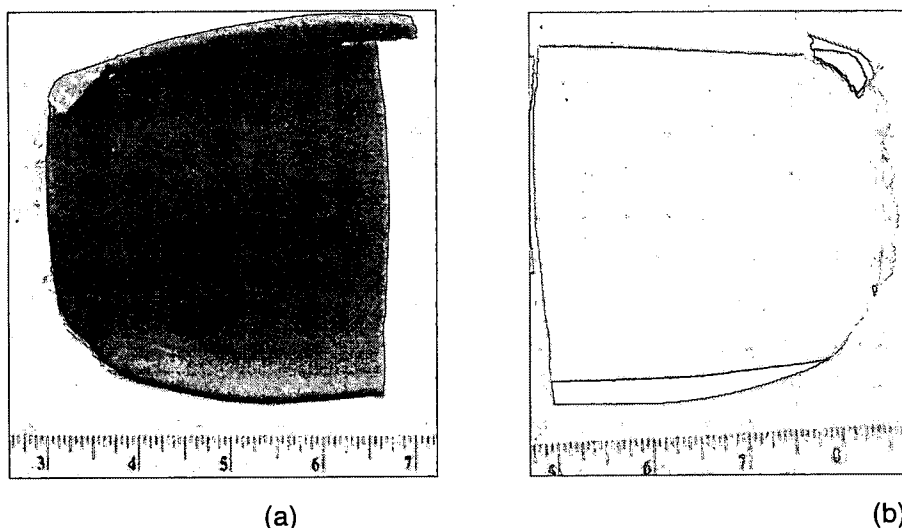


Figure 4.24: Photographs of green bi-layer tape with 50 wt% graphite: (a) graphite side and (b) the YSZ side.

The top side in this row is the porous layer. During the sintering process the porous layer tends to shrink more, thus creating a curved surface. The bi-layer specimens sintered at 1350°C for 2 hours and subsequently resintered at 1550°C for 2 hours are shown in Row C. These sintered specimens are flat. Thus, it is quite apparent that a two-step sintering is required to obtain flat bi-layer specimens.

Table 4.5 presents geometrical attributes of the single and bi-layer specimens containing 45, 50, and 55 wt% graphite before and after sintering. It is noted that a single layer tends to shrink more as compared to the bi-layer and shrinkage increases with increasing graphite concentration. Mechanical strength also decreases with the increase in graphite content.

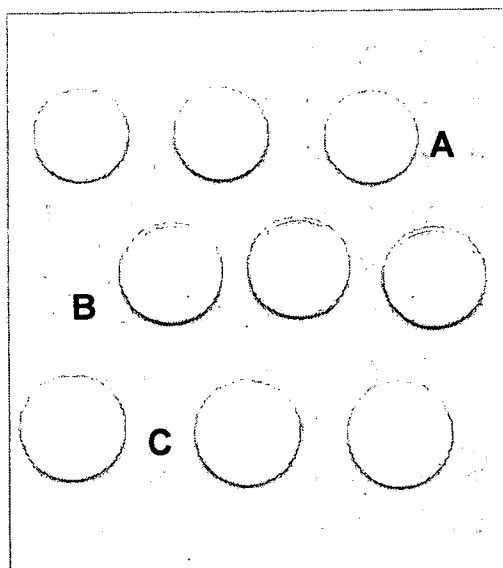


Figure 4.25: Photograph of sintered disc specimen (16 mm): Row A – single layer, porous YSZ sintered at 1550°C for 4 hours; Row B – bi-layer sintered at 1550°C for 4 hours, porous layer on top; Row C - bi-layer sintered at 1350°C for 2 hours and then at 1550°C for 2 hours.

Table 4.5: Geometrical Characteristics of Single and Bi-Layers Before and After sintering

Tape Description	Single Layer			Bi-layer on the Top of Pure YSZ			
	Diameter (mm)		Shrinkage (%)	Diameter (mm)		Shrinkage (%)	Qualitative Mechanical Strength
	Before Sintering	After Sintering		Before Sintering	After Sintering		
YSZ + 45% G	16.01	11.20	30.0	16.01	12.07	24.6	Good
YSZ + 50% G	16.01	11.07	30.9	16.01	12.01	25.0	Weak
YSZ + 55% G	16.01	10.99	31.4	16.01	12.0	25.0	Bad

4.7. Fabrication of direct hydrocarbon solid oxide fuel cells (DHSOFCs)

Four YSZ bi-layer specimens were fabricated using the tape casting process. The porous sides of these specimens were infiltrated with various fractions of CeO_2 and Cu. The YSZ - CeO_2 - Cu composite would serve as anode of the cell. The attributes of these specimens are presented in Table 4.6. The ratio (by volume) of CeO_2 : Cu varied from 1:0.93 to 1:2.34. After introduction of CeO_2 and Cu in the porous layer, the porosity of the anodic layer remained in the range of 30 to 36%, which is sufficient for storage and diffusion of fuel. The anode and electrolyte sides of these specimens are shown in Figure 4.26. Subsequent to the preparation of the anode side, an interlayer (YSZ : LSM = 1:1, on weight basis) and cathodic layer [LSM + Graphite (10 wt%)] were applied and fired independently. The inter and cathodic layers were fired at 1200°C (2 hours) and 1175°C (2 hours), respectively. The anode and cathode sides of the four specimens obtained after complete processing is shown in Figure 4.27. The specimens are free of cracks.

Table 4.6: Properties and Constitution of Direct Oxidation SOFC bi-layer Specimens

Specimen No.	Vol% of YSZ	Vol% of Pores*	Vol% of CeO_2	Vol% of Cu	Vol% Pores**	Ratio of Ceria and Cu Vol%
1	36.29	49.97	4.11	9.63	36.23	1:2.34
2	36.29	47.03	5.02	11.66	30.35	1:2.32
3	36.29	47.88	8.19	7.64	32.05	1:0.93
4	36.29	49.10	6.27	8.34	34.49	1:1.33

*Before CeO_2 and Cu infiltration

**After CeO_2 and Cu infiltration

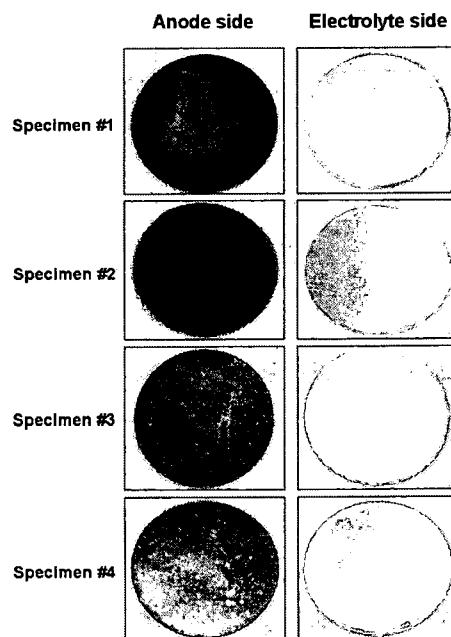


Figure 4.26: Photographs of anodic (after CeO_2 and Cu infiltration) and electrolyte sides of the four specimens.

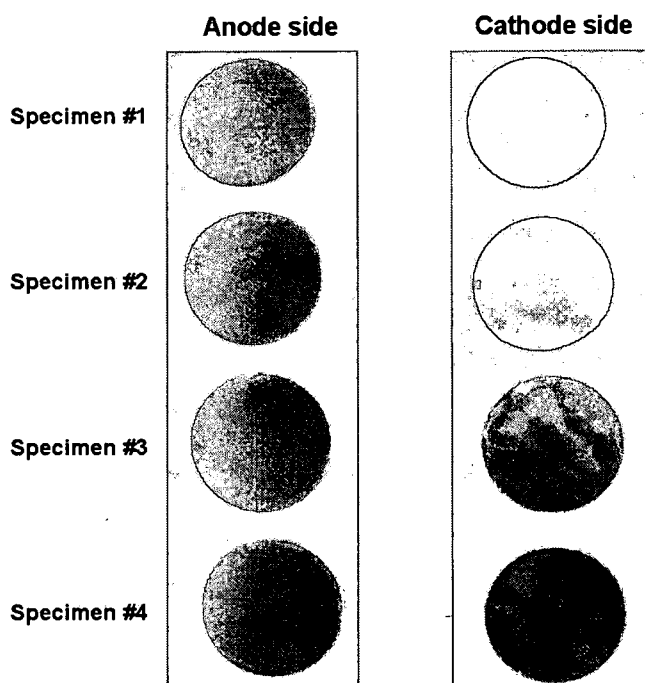


Figure 4.27: Photographs of anodic (CeO_2 and Cu) and cathodic (interlayer + LSM) sides of the four specimens.

Prior to the test, the cells were coated with platinum paste and fired at 980°C for 30 minutes. It diffused well with anode and cathode of the cell. Platinum lead wires were attached to the platinized electrodes and fired at 980°C for 30 minutes. The platinum electrode application and heating processes were modified such that the platinum paste after firing covers the platinum wire and provides a good bonding of the platinum wire to the electrode.

4.8 Testing of direct hydro carbon solid oxide fuel cell (DHSOFC)

The testing of DHSOFC involves several steps. The fuel cell must be cemented on a ceramic tube that provides the inlet for fuel and outlet for exhaust gases. The test fixture is subsequently placed in a high temperature furnace before measuring electrical performance of the cell.

4.8.1 The test fixture

The design of the test fixture is shown in Figure 4.29. It consists of two components:

- (1) an alumina tube on which the cell containing platinum wires is mounted
- (2) a Macor[®] cap which is inserted in the alumina tube for fuel delivery on the anodic side of the cell. The Macor[®] cap also contains a tube for the exit of exhaust gases. The photographs of these two components of fixture are shown in Figure 4.30(a, b). After attachment of the platinum lead wires to the cell, it was cemented to the one end of the ceramic tube. The other side of the ceramic tube was fitted with the Macor[®] cap for fuel inlet and exhaust outlet. Photographs of the ceramic tube with the attached cell and fuel inlet/outlet are shown in Figure 4.30c.

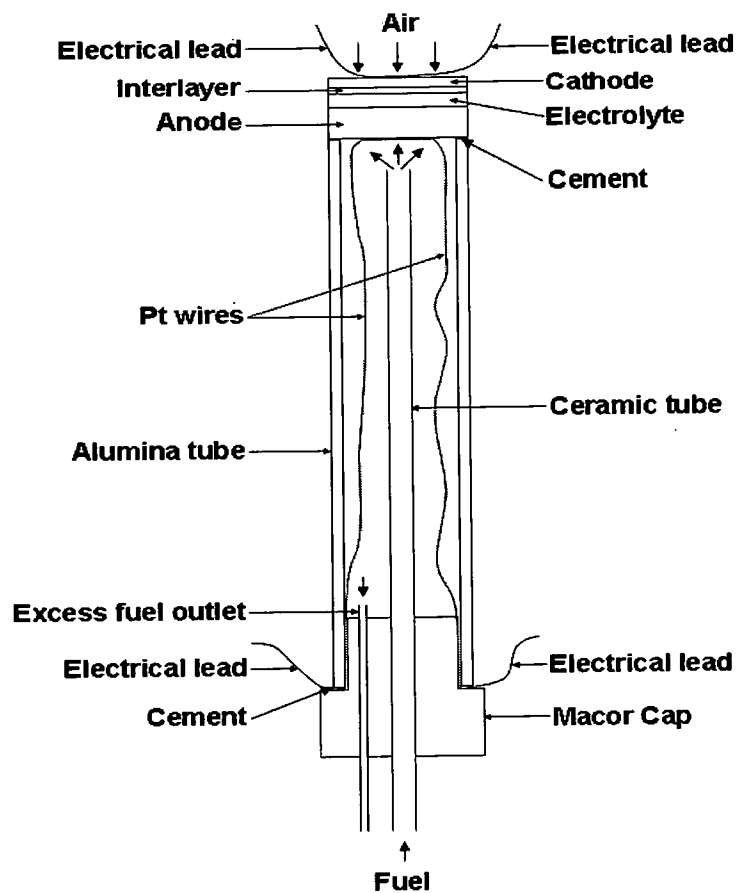


Figure 4.29: Schematic design of a SOFC test fixture.

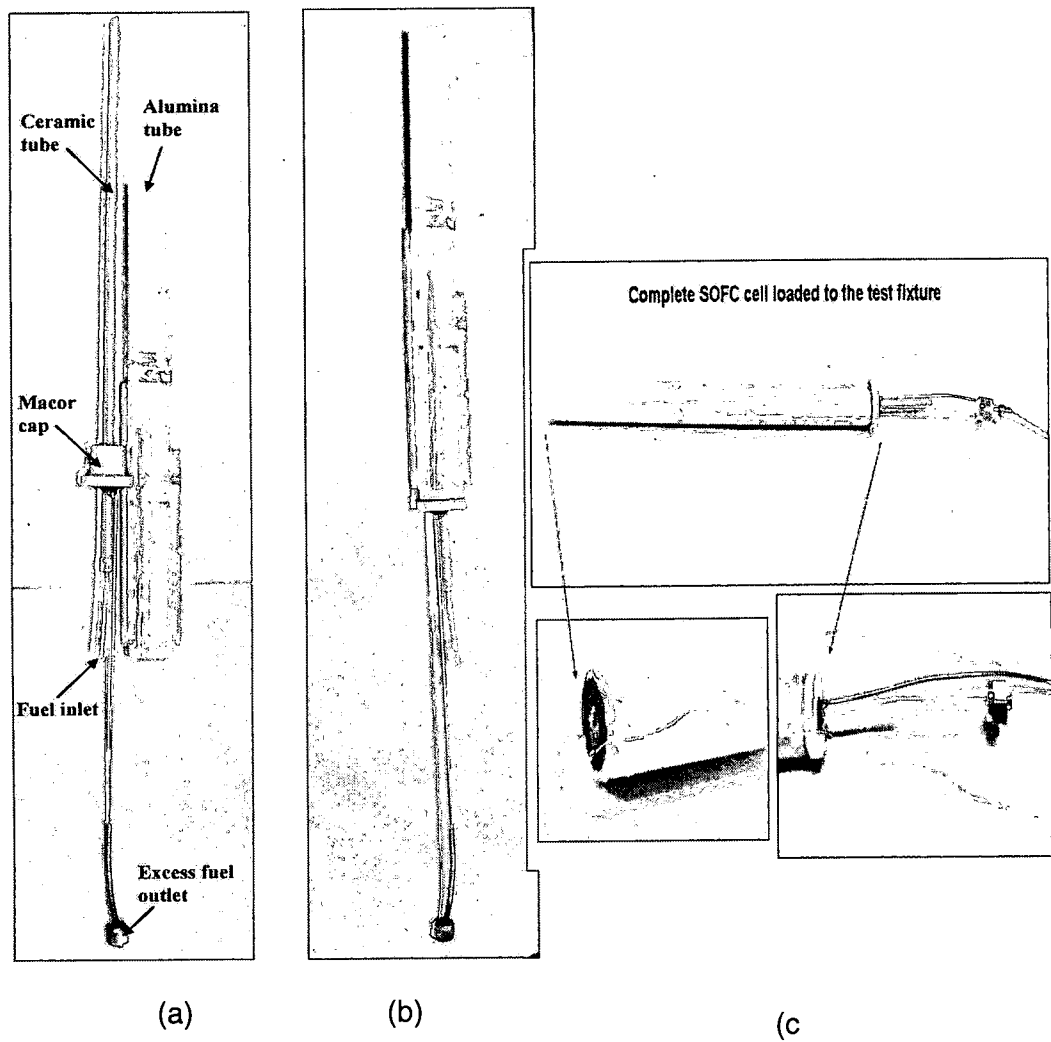


Figure 4.30: Fixture components: (a) unassembled (b) assembled (c) fuel cell cemented to the fixture

4.8.2 The polarization measurement of DHSOFC

The test fixture loaded with DHSOFC is placed in the furnace to test the performance of the cell. The fuel supply was started and the temperature of the furnace was raised slowly and simultaneously. At higher temperatures (700 °C) efforts were made to get performance curves. Initially many cells cracked during this evaluation process.

The cell fracture was recognized as a technical issue. This issue was addressed by a) increasing the thickness of the electrolyte layer, and b) making use of the composite (YSZ- Al_2O_3) electrolyte. By adding alumina, Al_2O_3 (20 wt %) to YSZ the mechanical strength of cells is increased and minimized the fracture of the cell. A new cell was made by increasing the thickness of the electrolyte to 165 μm consisting of YSZ and alumina (Al_2O_3) instead of only YSZ.

The cell comprising of the YSZ- Al_2O_3 electrolyte and consisting of 11.85 wt% of CeO_2 and 24.16 wt% of Cu in the anode was tested using hydrogen as fuel. Performance of the fuel cell can be summarized with a graph of its current – voltage characteristics. This graph is called a current-voltage (I -V) curve. Fuel cells are generally operated at or just below the peak power density value and one can obtain this value from power density curve. The power density curve is obtained by multiplying the voltage at each point on the I-V curve by the corresponding current density. Fuel cell power density increases with increasing current density, reaches a maximum, and then falls at yet higher current densities. The I -V curve with power density curve of the anode-supported cell operated at 800 °C and 850 °C are presented in Figures 4.31 and 4.32

respectively. The power density reaches a peak value at current density of 0.09 A/cm^2 when operated at 800°C . At this point the cell voltage is 0.4 V and peak power density is 33mW/cm^2 . When operated at 850°C , the power density reaches a peak value at current density of 0.12 A/cm^2 . At this point the cell voltage is 0.35 V and peak power density is 40mW/cm^2 . From this data we can infer that peak power density and range of current density increases with the increase in the operating temperature.

The open circuit voltage (OCV) of ideal fuel cell is about 1.2 volts . But during the initial stages of the operation of the fuel cell, some energy is utilized to activate the electrochemical reactions; because of this, when the fuel cell was operated at 800°C , it registered only 0.76 V . This difference in the OCV is called activation overpotential. We can minimize activation overpotential by operating the fuel cell at higher temperature. The same was observed when the fuel cell was operated at higher temperature (i.e. at 850°C). At this temperature it registered the OCV of 0.83 V and thereby activation overpotential decreases. The value of the activation overpotential can further be decreased by further increasing the operating temperature, but it would be desirable to keep the operating temperature as low as possible so that inexpensive materials can be used to make the other parts of the SOFC. The activation overpotential can also be decreased by operating at the same temperature if distribution of reactants and products can be homogenized in the structure of the cell.

From Figures 4.31 and 4.32 we can say that I-V curves are linear. The slope of these curves corresponds to primarily resistance of the electrolyte

membrane. Steeper is the slope, higher is the resistance. The increase in the peak power density can also be achieved by minimizing the electrolyte resistance. The electrolyte resistance can be decreased by decreasing its thickness. However, its thickness cannot be decreased beyond the value at which the cell might fracture during its operation. Therefore, optimization of the electrolyte membrane thickness and also its composition is essential to optimize the performance of the cell.

The fuel cell cannot be tested on hydrocarbon fuels as the experimental set up was not ready when this work was completed.

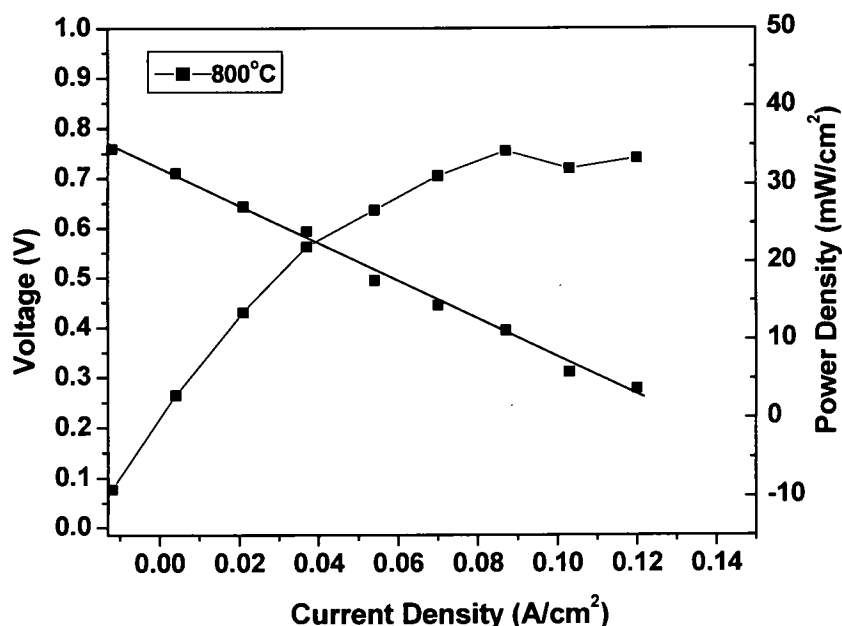


Figure 4.31: I – V curve and power density curve of DHSOFC (Cu and CeO_2 anode) operated at $800^\circ C$.

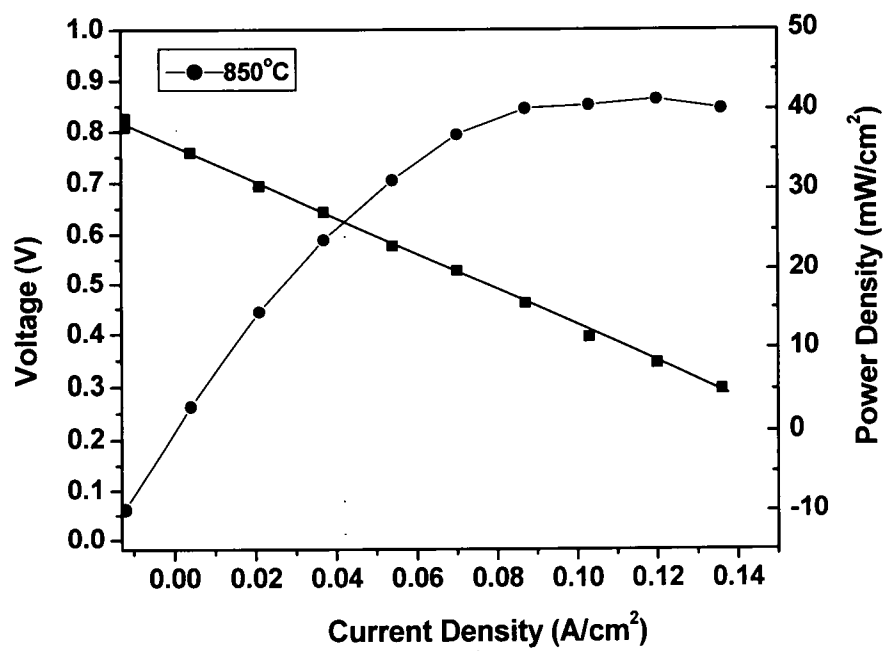


Figure 4.32: I – V curve and power density curve of DHSOFC (Cu and CeO₂ anode) operated at 850°C.

CHAPTER V

SUMMARY AND CONCLUSIONS

This thesis relates to the development of direct hydrocarbon solid oxide fuel cells (DHSOFC). The development included processing of anodic component, fabrication of bi-layers, deposition of an interlayer and incorporation of the cathode. For this investigation tape casting process was employed to prepare single and bi-layers of YSZ. Two pore formers, rice flour and graphite, were evaluated for their effectiveness. The sintering parameters were optimized to control structure and volume fraction of pores so as to infiltrate desirable amounts of Cu and CeO_2 . Electrical properties of the single layer YSZ cermet were evaluated. The results were utilized to prepare complete DHSOFC. The performance of the cell was evaluated using hydrogen as the fuel. Significant conclusions of the investigation are summarized in the following paragraphs:

- The resistance of the YSZ-Ni cermet that was prepared by using the porous YSZ (rice flour as pore former) is around $2\ \Omega$ at $850\ ^\circ\text{C}$ where as for the YSZ-Ni cermet prepared by using graphite as pore former is around $0.16\ \Omega$ at room temperature. The high resistance of the former cermet was because of discontinuity of Ni which resulted from the poor connectivity of the pores. The

lower resistance of the later cermet was attributed to the better connectivity of the pores and also better connectivity of Ni. This improved connectivity of the pores is important for diffusion of the fuels and is believed to be related to the usage of graphite as pore former. Therefore, graphite was used as pore former for further investigation.

- The sintering of bi-layer tapes at 1400 °C for 4 hrs and 1500 °C for 1 hr was insufficient to fully densify the dense layer. When the bi-layer specimens were sintered at 1550 °C for 4 hrs, the porosity of dense layer was around 1.5 % comprising of only closed pores which was deemed acceptable for fabricating a working SOFC cell. The porosity of the porous layer was less than 35 %. The low porosity issue was addressed by increasing the graphite content. At higher weight percentages of graphite (50 wt %) content the specimens became fragile and disintegrated during handling. Therefore, 45 wt% of graphite is considered as optimum wt% as it provided mechanically strong bi-layer with porous layer having porosity of 64.15%. Flat bi-layer specimens were obtained by two-step sintering i.e. by heat treatment at 1350 °C for 2 hrs and at 1550 °C for 2 hrs.

- The AC impedance measurements were conducted in the temperature range of -60 to 25 °C on the porous YSZ-Cu cermet containing 4.31, 5.89, 7.88 and 9.84 vol% of Cu. The results showed that the specimen containing 5.89 vol% of copper has higher conductivity of 0.35 S/cm and the electronic transport number

of 0.72. From this result it is expected to obtain superior performance of the DHSOFC containing 5.89 vol% of Cu.

- The porous YSZ specimens containing [(0, 5.90), (2.56, 6.75), (5.12, 7.7), (7.39, 8.26)] vol% of CeO₂ and Cu were evaluated by measuring the conductivity and electronic transport numbers and found that the conductivity was higher and the activation energy was lower for the cermet with 7.39 vol% of CeO₂ and electronic transport number was higher for the cermet with 5.12 vol% of CeO₂.
- Porous sides of the YSZ bi-layer specimens were infiltrated with various fractions of CeO₂ and Cu, which served as anode of the cell. The ratio (by volume) of CeO₂ : Cu varied from 1:0.93 to 1:2.34. Subsequent to the preparation of the anode side, an interlayer (YSZ : LSM = 1:1, on weight basis) and then the cathodic layer [LSM + graphite (10 wt %)] were applied and fired independently on to the dense side. During the evaluation process, the fuel cells fractured and this technical issue was addressed a) by increasing the thickness of the electrolyte and b) by making use of the composite (YSZ-Al₂O₃) electrolyte. By adding alumina (Al₂O₃, 20 wt %) to YSZ the mechanical strength of the cells increased and minimized the fracture of the cell. The fuel cell comprising of the YSZ-Al₂O₃ electrolyte and consisting of 11.85 wt% of CeO₂ and 24.16 wt% of Cu in the anode was tested using hydrogen as the fuel. The fuel cell exhibited peak power densities of 33 and 40 mW/cm² at 800 and 850 °C respectively. The open circuit voltage (OCV) of 0.76V was measured at 800 °C. The OCV was increased

to 0.83V by increasing the operating temperature to 850 °C. However, the OCV is much lower than the theoretical OCV of 1.2 V of an ideal SOFC. The lower OCV is attributed to the activation overpotential.

In the future these DHSOFCs will be tested using the hydrocarbon fuels as the experimental setup was not ready when this experimental work was completed.

REFERENCES

1. Bartholomew, C.H.; *Catl. Rev. Sci. Eng.* **1982**, 24, 67.
2. Baker, R. T. K.; *Carbon*, **1989**, 27, 315.
3. Steele, B. C. H.; *Solid State Ionics*, **1996**, 86-88, 1223.
4. Hernadi, K.; Fonseca, A.; Nagy, J. B.; Siska, A.; and Kiricsi, I.; *Appl. Catal.*, A, **2000**, 199, 245.
5. Gorte, R.J.; Vohs, J.M.; McIntosh, S.; *Solid State Ionics*, **2004**, 175,1.
6. Steele, B.C.H. *Philos. Trans. R. Soc. London A* **1996**, 354, 1695.
7. Wang, X.; Nakagawa, N.; Kato, K. *J. Electrochem. Soc.* **2001**, 148, A565.
8. Mizusaki, J.; Tagawa, H.; Tsuneyoshi, K.; Sawata, A. *J. Electrochem. Soc.* **1991**, 138, 1867.
9. de Haart, L. G. J.; Kuipers, R. A.; de Vries, K. J.; Burggraaf, A. J. J. *Electrochem. Soc.* **1991**, 138, 1970.
10. Østergård, M. J. L.; Mogensen, M. *Electrochim. Acta* **1993**, 38, 2015.
11. Fukunaga, H.; Ihara, M.; Sakaki, K.; Yamada, K. *Solid State Ionics* **1996**, 86-88, 1179.
12. Tanner, C. W.; Fung, K.-Z.; Virkar, A. V. *J. Electrochem. Soc.* **1997**, 22, 144.
13. Brown, M.; Primdahl, S.; Mogensen, M. *J. Electrochem. Soc.* **2000**, 475, 147.
14. Virkar, A. V.; Fung, K. Z.; Tanner, C. W. U.S. Patent No. 5,543,239, 1996.
15. Fleig, J. J. *Power Sources* **2002**, 105, 228.
16. Erbstritt, D.; Müller, A. C.; Weber, A.; Ivers-Tiffée, E. In *SOFC VIII*; Singhal, S. C., Dokiya, M., Eds.; The Electrochemical Society Proceedings Series PV 2003-07; The Electrochemical Society: Pennington, NJ, 2003; p 1330.
17. Yokokawa, H. *Annu. Rev. Mater. Res.* **2003**, 33, 581.

18. Kleveland, K.; Einarsrud, M.-A.; Schmidt, C. R.; Shamsili, S.; Faaland, S.; Wiik, K.; Grande, T. *J. Am. Ceram. Soc.* **1999**, *82*, 729.
19. Colomer, M. T.; Steele, B. C. H.; Kilner, J. A. *Solid State Ionics* **2002**, *147*, 41.
20. Simner, S. P.; Bonnett, J. F.; Canfield, K. D.; Shelton, J. P.; Sprenkle, V. L.; Stevenson, J. W. *J. Power Sources* **2003**, *113*, 1.
21. EG&G Technical Services, Inc. *Fuel Cell Handbook 6th Edition*; DOE/NETL-2002/1179; U.S. Department of Energy, Office of Fossil Energy, National Energy Technology Laboratory: Morgantown, WV; p 2.1-2.26
22. Liu, J.; Madsen, B. D.; Ji, Z.; Barnett, S. A. *Electrochem. Solid-State Lett.* **2002**, *5*, A122.
23. Murray, E. P.; Tsai, T.; Barnett, S. A. *Nature* **1999**, *400*, 649.
24. Murray, E. P.; Barnett, S. A. In *SOFC VI*; Singhal, S. C., Dokiya, M., Eds.; The Electrochemical Society Proceedings Series PV 1999-19; The Electrochemical Society: Pennington, NJ, 1999; p 1001.
25. Liu, J.; Barnett, S. A. *Solid State Ionics* **2003**, *158*, 11.
26. Zhan, Z.; Madsen, B. D.; Liu, J.; Barnett, S. A. In *SOFC VIII*; Singhal, S. C., Dokiya, M., Eds.; The Electrochemical Society Proceedings Series PV 2003-07; The Electrochemical Society: Pennington, NJ, 2003; p 1286.
27. Park S., Craciun R., Vohs J.M., Gorte R.J., *J. Electrochem. Soc.*, Volume: 146, Issue: 10 (1999), pp. 3603
28. Park S., Vohs J.M., Gorte R.J., *Nature*, Volume: 404, (2000), pp. 265
29. Gorte R.J., Park S., Vohs J.M., Wang C., *Adv. Mater.*, Volume: 12, Issue: 19 (2000), pp. 1465
30. Park S., Gorte R.J., Vohs J.M., *J. Electrochem. Soc.*, Volume: 148, Issue: 5 (2001), pp. A443
31. Steven McIntosh, John M. Vohs, Raymond J. Gorte, *Electrochimica Acta* *47* (2002) 3815-3821.
32. Gorte R.J., Vohs J.M., *J.Catal.* 2003, *216*, 477.

R002593382